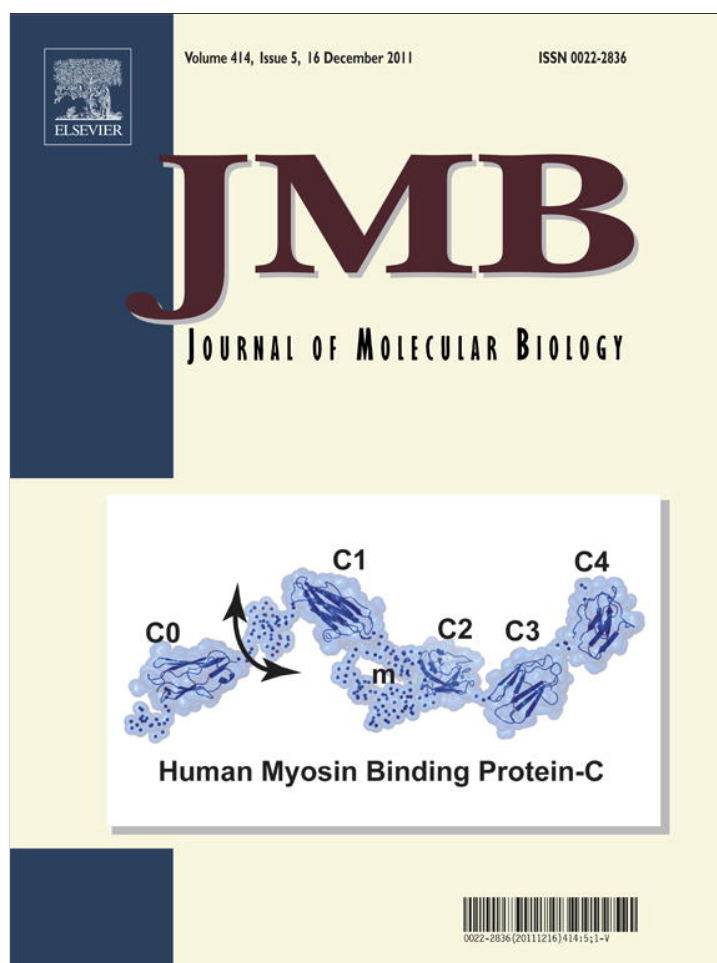


# A Three-Dimensional FRET Analysis to Construct an Atomic Model of the Actin-Tropomyosin Complex on a Reconstituted Thin Filament

メタデータ	言語: English 出版者: 公開日: 2012-01-24 キーワード (Ja): キーワード (En): 作成者: MIKI, Masao, MAKIMURA, Satoshi, SAITOH, Takahiro, BUNYA, Masashi, SUGAHARA, Yasuyuki, UENO, Yutaka, KIMURA-SAKIYAMA, Chieko, TOBITA, Hidetaka メールアドレス: 所属:
URL	<a href="http://hdl.handle.net/10098/4852">http://hdl.handle.net/10098/4852</a>



This article appeared in a journal published by Elsevier. The attached copy is furnished to the author for internal non-commercial research and education use, including for instruction at the authors institution and sharing with colleagues.

Other uses, including reproduction and distribution, or selling or licensing copies, or posting to personal, institutional or third party websites are prohibited.

In most cases authors are permitted to post their version of the article (e.g. in Word or Tex form) to their personal website or institutional repository. Authors requiring further information regarding Elsevier's archiving and manuscript policies are encouraged to visit:

<http://www.elsevier.com/copyright>



# A Three-Dimensional FRET Analysis to Construct an Atomic Model of the Actin–Tropomyosin Complex on a Reconstituted Thin Filament

Masao Miki<sup>1\*</sup>, Satoshi Makimura<sup>1</sup>, Takahiro Saitoh<sup>1</sup>, Masashi Bunya<sup>1</sup>, Yasuyuki Sugahara<sup>1</sup>, Yutaka Ueno<sup>2</sup>, Chieko Kimura-Sakiyama<sup>1</sup> and Hidetaka Tobita<sup>3</sup>

<sup>1</sup>Division of Applied Chemistry and Biotechnology, Graduate School of Engineering Science, University of Fukui, Fukui 910-8507, Japan

<sup>2</sup>Biomedical Research Institute, National Institute of Advanced Industrial Science and Technology, Tsukuba 305-8568, Japan

<sup>3</sup>Division of Materials Science and Engineering, Graduate School of Engineering Science, University of Fukui, Fukui 910-8507, Japan

Received 9 August 2011;  
received in revised form  
17 October 2011;  
accepted 19 October 2011  
Available online  
25 October 2011

Edited by R. Craig

## Keywords:

troponin;  
tropomyosin;  
three-dimensional FRET  
analysis;  
muscle thin filament;  
Ca<sup>2+</sup> regulation

Fluorescence resonance energy transfer (FRET) was used to construct an atomic model of the actin–tropomyosin (Tm) complex on a reconstituted thin filament. We generated five single-cysteine mutants in the 146–174 region of rabbit skeletal muscle  $\alpha$ -Tm. An energy donor probe was attached to a single-cysteine Tm residue, while an energy acceptor probe was located in actin Gln41, actin Cys374, or the actin nucleotide binding site. From these donor–acceptor pairs, FRET efficiencies were determined with and without Ca<sup>2+</sup>. Using the atomic coordinates for F-actin and Tm, we searched all possible arrangements for Tm segment 146–174 on F-actin to calculate the FRET efficiency for each donor–acceptor pair in each arrangement. By minimizing the squared sum of deviations for the calculated FRET efficiencies from the observed FRET efficiencies, we determined the location of the Tm segment on the F-actin filament. Furthermore, we generated a set of five single-cysteine mutants in each of the four Tm regions 41–69, 83–111, 216–244, and 252–279. Using the same procedures, we determined each segment's location on the F-actin filament. In the best-fit model, Tm runs along actin residues 217–236, which were reported to compose the Tm binding site. Electrostatic, hydrogen-bonding, and hydrophobic interactions are involved in actin and Tm binding. The C-terminal region of Tm was observed to contact actin more closely than did the N-terminal region. Tm contacts more residues on actin without Ca<sup>2+</sup> than with it. Ca<sup>2+</sup>-induced changes on the actin–Tm contact surface strongly affect the F-actin structure, which is important for muscle regulation.

© 2011 Elsevier Ltd. All rights reserved.

\*Corresponding author. E-mail address: [mmiki@u-fukui.ac.jp](mailto:mmiki@u-fukui.ac.jp).

Present address: C. Kimura-Sakiyama, Division of Biological Science, Graduate School of Science, Nagoya University, Furo, Nagoya, Japan.

Abbreviations used: FRET, fluorescence resonance energy transfer; Tm, tropomyosin; Tn, troponin; 3D-EM, three-dimensional electron microscopy; S1, myosin subfragment 1; IAEDANS, 5-(2-iodoacetylaminophenyl)aminonaphthalene 1-sulfonic acid; AEDANS, 5-((acetylaminophenyl)amino)naphthalene-1-sulfonate; DABMI, 4-dimethyl-aminophenylazophenyl 4'-maleimide; FLC, fluorescein cadaverine; TNP, 2'-(or 3')-O(2,4,6-trinitrophenyl); DAB-F-actin, DABMI-labeled F-actin.

## Introduction

Striated muscle contraction is regulated by tropomyosin (Tm) and troponin (Tn) in the actin filament in response to changes in  $\text{Ca}^{2+}$  concentration.<sup>1</sup> Rabbit skeletal muscle  $\alpha$ -Tm, a 284-residue dimeric coiled-coil protein, contains seven quasi-equivalent regions and spans seven actin monomers along the two-start long-pitch F-actin helix.<sup>2</sup> Tn consists of three subunits: TnT, TnI, and TnC. The crystal structures of actin,<sup>3</sup> Tm,<sup>4</sup> and the Tn core domain<sup>5,6</sup> have been solved. Since the thin filament is composed of hundreds of actin, Tm, and Tn molecules, it is difficult to crystallize such supramolecular assemblies. The atomic structure of G-actin was modeled into the actin filament helix using X-ray diffraction patterns from aligned actin filament gels.<sup>7,8</sup> However, it is unclear how the Tm–Tn complex covers the seven actin monomers in the thin filament and how the conformation changes occur in the thin filament during activation by  $\text{Ca}^{2+}$  binding to Tn. To date, the structural models of the thin filament have been constructed primarily using image reconstructions from three-dimensional electron microscopy (3D-EM) and X-ray diffraction measurements.<sup>9–12</sup> To use the helical symmetry of the thin filament in analyses, we assumed that the seven quasi-equivalent regions of Tm interact equivalently with each of the seven actin monomers and that the Tn mass, which is approximately equal to the Tm mass, was effectively averaged over the structure. Using a single-particle analysis of 3D-EM data, Narita *et al.* reported that each of the seven Tm regions binds actin in a slightly different manner.<sup>11</sup> Although the atomic structure of the Tn core domain has been determined, it is only part of the larger Tn molecule (~60% of the mass). Therefore, it is difficult to evaluate precisely the contribution of Tn to the 3D-EM and X-ray diffraction analyses. Given the current lack of detailed structural information for Tn and Tm on the thin filament, previous studies on the structure of the thin filament and its conformational changes upon  $\text{Ca}^{2+}$  binding are ambiguous.<sup>2,13</sup>

Fluorescence resonance energy transfer (FRET) spectroscopy, an optical ruler for measuring distance in the range of 10–70 Å, has been extensively used to study muscle proteins.<sup>14,15</sup> This method is especially valuable for detecting small conformational changes (even a few angstroms of distance change), since transfer efficiency is a function of the inverse of the sixth power of the distance between probes. FRET between probes on Tn and actin has shown a large  $\text{Ca}^{2+}$ -induced and myosin subfragment 1 (S1)-induced change in the transfer efficiencies suggesting Tn conformation changes on the actin filament in response to the three states of the thin filament.<sup>15</sup> On the other hand, FRET between probes on Tm and actin has not shown any

significant  $\text{Ca}^{2+}$ -induced change in the transfer efficiencies.<sup>15–19</sup> However, interpretation of the data regarding the  $\text{Ca}^{2+}$ -induced Tm movement on F-actin is controversial. One interpretation states that absence of change in the transfer efficiency shows absence of Tm movement, but the other interpretation states that Tm moves between two positions on the actin filament, giving the same transfer efficiency to each other so that the  $\text{Ca}^{2+}$ -induced Tm movement does not accompany the change in the transfer efficiency. In these previous experiments, the transfer efficiency for each donor–acceptor pair was analyzed separately, leaving ambiguous the evaluation of the three-dimensional positional change. On the other hand, we systematically measured numerous intermolecular FRET efficiencies between probes on Tn subunits and Tm on the reconstituted thin filament. We then constructed an atomic model of the Tn core domain and the Tm complex by performing a global search for the crystal structure's rigid-body movements to determine the position and the orientation that minimize deviations between the calculated and the observed FRET efficiencies.<sup>20</sup> Because one Tm molecule winds around seven actin monomers along the long-pitch helix of the filament, it is impossible to use the rigid-body movements for the full-length Tm molecule on the F-actin filament without changing the Tm crystal structure. Therefore, the Tm molecule was divided into several short segments (28 residues), and each segment was placed on the F-actin filament using the crystal structure's rigid-body movements. Herein, we determined the transfer efficiencies between the probes that were attached to Tm and the probes that were attached to actin using 30 different measurements for each Tm segment (41–69, 83–111, 146–174, 216–244, and 252–279). The atomic coordinates of Lorenz *et al.*'s<sup>8</sup> F-actin model and the pig skeletal Tm crystal structure (Protein Data Bank code: 1C1G)<sup>4</sup> were used. By systematically translating and rotating each Tm segment around F-actin, we obtained the best-fit models with and without  $\text{Ca}^{2+}$  for each Tm segment by minimizing the squared sum of deviations of the calculated energy transfer efficiencies from the observed values for all of the FRET measurements at each orientation. The three-dimensional analysis of FRET data herein allows for a detailed model of the thin filament structure.

## Results

5-(2-Iodoacetyl aminoethyl) aminonaphthalene 1-sulfonic acid (IAEDANS) was attached to each cysteine in the single-cysteine Tm mutants at positions 146, 153, 160, 167, and 174 in the 146–174 region; at positions 41, 48, 55, 62, and 69 in the 41–69 region; at positions 83, 90, 97, 104, and 111 in the 83–

111 region; at positions 216, 223, 230, 237, and 244 in the 216–244 region; and at positions 252, 258, 265, 272, and 279 in the 251–279 region as an energy donor molecule called 5-(((acetylamino)ethyl)amino)naphthalene-1-sulfonate (AEDANS) (IAEDANS after reaction with a sulfhydryl group). To examine whether the AEDANS-labeled Tm mutants maintained native Tm activity, we measured the  $\text{Ca}^{2+}$  regulation of actin-activated S1-ATPase activity for the labeled Tm mutants (Fig. S1 in Supplementary Information).  $\text{Ca}^{2+}$  sensitivity is defined as  $\{1 - (\text{Activity}_{-\text{Ca}} / \text{Activity}_{+\text{Ca}})\} \times 100$ . The labeled Tm mutants exhibited almost the same  $\text{Ca}^{2+}$  sensitivity as the native Tm (rabbit  $\alpha$ -Tm). The relative  $\text{Ca}^{2+}$  sensitivity (percentage of native Tm sensitivity) of each AEDANS-labeled Tm mutation is shown in Tables 1–5. The energy acceptor molecules 4-dimethyl-aminophenylazophenyl 4'-maleimide (DABMI) and fluorescein cadaverine (FLC) were attached to actins Cys374 and Gln41, respectively, and the ADP bound to F-actin was replaced with 2'(or 3')-O-(2,4,6-trinitrophenyl) (TNP)

ADP. Labeling F-actin with these acceptor probes did not impair  $\text{Ca}^{2+}$  sensitivity in the thin filaments.

### FRET between the probes attached to Tm and the probes attached to F-actin on the reconstituted thin filament

The transfer efficiencies between AEDANS–Tm and FLC–F-actin were determined by measuring the donor fluorescence intensity with and without the acceptor. The solvent used for these experiments was buffer F [60 mM KCl, 2 mM  $\text{MgCl}_2$ , 20 mM Tris–HCl (pH 7.6), and 1 mM  $\text{NaN}_3$ ] and either 50  $\mu\text{M}$   $\text{CaCl}_2$  for the  $+\text{Ca}^{2+}$  state or 1 mM ethylene glycol bis( $\beta$ -aminoethyl ether)  $N,N'$ -tetraacetic acid for the  $-\text{Ca}^{2+}$  state at 20 °C. The ratio of donor fluorescence quenching was measured by titrating AEDANS–Tm/Tn with FLC–F-actin in the presence and in the absence of  $\text{Ca}^{2+}$ , as described by Miki *et al.*<sup>18</sup> The excitation wavelength was 340 nm. Although the donor fluorescence maximum was found at 490 nm, emission was measured at 460 nm to avoid acceptor

**Table 1.** FRET between Tm segment 146–174 and F-actin on the reconstituted thin filament

Tm (D)	$Q_0$ (+Ca), $Q_0$ (–Ca)	Actin (A)	$R_0$ (+Ca), $R_0$ (–Ca)	A/P	$E_{\text{obs}}/E_{\text{calc}}$	
					+ $\text{Ca}^{2+}$	– $\text{Ca}^{2+}$
146 (85%)	0.258, 0.278	DAB	37.2, 37.7	0.50	0.24/0.25	0.32/0.30
				1.00	0.40/0.46	0.49/0.55
		TNP	37.9, 38.4	0.33	0.37/0.30	0.41/0.32
				0.42	0.48/0.43	0.51/0.45
		FLC	44.1, 44.7	0.56	0.37/0.40	0.43/0.44
153 (99%)	0.227, 0.231	DAB	36.4, 36.5	0.93	0.46/0.55	0.50/0.59
				0.50	0.29/0.24	0.32/0.26
		TNP	37.1, 37.2	1.00	0.46/0.44	0.49/0.47
				0.33	0.30/0.28	0.31/0.29
		FLC	43.2, 43.3	0.42	0.43/0.40	0.48/0.40
160 (112%)	0.298, 0.297	DAB	38.1, 38.1	0.56	0.44/0.41	0.44/0.43
				0.93	0.53/0.57	0.53/0.59
		TNP	38.8, 38.8	0.50	0.31/0.27	0.32/0.27
				1.00	0.47/0.46	0.49/0.46
		FLC	45.2, 45.2	0.33	0.34/0.29	0.39/0.29
167 (99%)	0.281, 0.275	DAB	37.8, 37.6	0.42	0.46/0.39	0.55/0.40
				0.56	0.41/0.46	0.46/0.47
		TNP	38.5, 38.3	0.93	0.48/0.63	0.51/0.64
				0.50	0.26/0.25	0.27/0.25
		FLC	44.8, 44.6	1.00	0.41/0.42	0.42/0.42
174 (104%)	0.239, 0.253	DAB	36.7, 37.1	0.33	0.33/0.26	0.33/0.27
				0.42	0.38/0.36	0.38/0.38
		TNP	37.4, 37.8	0.56	0.42/0.43	0.42/0.43
				0.93	0.47/0.60	0.47/0.60
		FLC	43.6, 44.0	0.50	0.27/0.22	0.30/0.24
				1.00	0.40/0.39	0.43/0.44
				0.33	0.31/0.27	0.36/0.31
				0.42	0.50/0.38	0.58/0.44
				0.56	0.42/0.38	0.42/0.41
				0.93	0.48/0.54	0.48/0.58

In the leftmost column, the percentage denoted beside the Tm residue number shows relative  $\text{Ca}^{2+}$  sensitivity (100% for native Tm), as defined in the text.

$Q_0$ , the quantum yield of AEDANS attached to Tm on the reconstituted thin filament in the presence of  $\text{Ca}^{2+}$  (+Ca) and in the absence of  $\text{Ca}^{2+}$  (–Ca);  $R_0$ , Förster's critical distance (Å); A/P, acceptor/protein (actin) labeling ratio;  $E_{\text{obs}}$ , measured energy transfer efficiency (errors in  $E_{\text{obs}}$  were within  $\pm 0.03$ );  $E_{\text{calc}}$ , calculated transfer efficiency at the best-fit model.

**Table 2.** FRET between Tm segment 41–69 and F-actin on the reconstituted thin filament

Tm (D)	$Q_0$ (+Ca), $Q_0$ (–Ca)	Actin (A)	$R_0$ (+Ca), $R_0$ (–Ca)	A/P	$E_{\text{obs}}/E_{\text{calc}}$	
					+Ca <sup>2+</sup>	–Ca <sup>2+</sup>
41 (101%)	0.234, 0.232	DAB	36.6, 36.6	0.5	0.29/0.25	0.25/0.25
				1	0.43/0.45	0.41/0.44
		TNP	37.1, 37.0	0.36	0.29/0.19	0.33/0.24
				0.45	0.33/0.23	0.35/0.29
				0.7	0.41/0.45	0.39/0.50
48 (83%)	0.227, 0.251	DAB	36.4, 37.0	0.82	0.48/0.51	0.48/0.55
				0.5	0.21/0.19	0.27/0.22
		TNP	36.9, 37.5	1	0.30/0.34	0.39/0.38
				0.36	0.23/0.21	0.30/0.26
				0.45	0.24/0.25	0.33/0.32
55 (113%)	0.230, 0.234	DAB	36.5, 36.6	0.7	0.33/0.44	0.47/0.52
				0.82	0.36/0.49	0.50/0.57
		TNP	37.0, 37.1	0.5	0.20/0.20	0.21/0.23
				1	0.32/0.36	0.36/0.39
				0.36	0.30/0.24	0.33/0.27
62 (113%)	0.236, 0.244	DAB	36.7, 36.9	0.45	0.33/0.30	0.38/0.33
				0.7	0.34/0.42	0.42/0.48
		TNP	37.2, 37.4	0.82	0.40/0.46	0.47/0.53
				0.5	0.25/0.23	0.29/0.25
				1	0.41/0.42	0.42/0.45
69 (85%)	0.251, 0.249	DAB	37.0, 37.0	0.36	0.29/0.24	0.29/0.27
				0.45	0.42/0.32	0.47/0.36
		TNP	37.5, 37.5	0.7	0.37/0.41	0.42/0.46
				0.82	0.47/0.45	0.50/0.51
				0.5	0.31/0.24	0.29/0.26
		DAB	37.0, 37.0	1	0.48/0.44	0.47/0.48
				0.36	0.36/0.25	0.37/0.27
		FLC	43.9, 43.8	0.45	0.40/0.33	0.40/0.36
				0.7	0.44/0.47	0.42/0.50
				0.82	0.54/0.52	0.53/0.55

FLC emission. To correct for fluorescence intensity changes from either F-actin binding or dilution effects, we added the same amount of nonlabeled F-actin to the AEDANS–Tm/Tn solution, and we took the ratio of the fluorescence intensities as the relative fluorescence intensity. The initial protein concentrations were 0.76  $\mu\text{M}$  Tm and 0.87  $\mu\text{M}$  Tn. FLC–F-actin absorption produced an inner-filter effect that resulted in an apparent decrease in fluorescence intensity, which was corrected.<sup>18,21</sup> The relative fluorescence intensity decreased with an increasing F-actin/Tm molar ratio of up to 7:1 and became nearly constant above a 7-fold excess of F-actin. The energy transfer efficiencies were obtained from saturation points. Two labeling ratios for the acceptor probes to F-actin were used. The observed transfer efficiency ( $E_{\text{obs}}$ ) and Förster's critical distance ( $R_0$ ) for each donor–acceptor pair are shown in Tables 1–5.

The FRET efficiencies between AEDANS–Tm and either DABMI-labeled F-actin (DAB–F-actin) or TNP-ADP–F-actin were determined by measuring the donor fluorescence intensity as described for FLC–F-actin. AEDANS emission was measured at 490 nm, as DAB–F-actin and TNP-ADP–F-actin do not fluoresce. Furthermore, the transfer efficiencies were determined using time-resolved single-photon counting, as contaminating emission from the

acceptor was entirely avoided in these cases and sufficient donor emission signal was obtained. Typical fluorescence decay curves for AEDANS–Tm with and without the acceptor (DAB) in the reconstituted thin filament are shown in Fig. S2.

The transfer efficiencies were determined by the lifetime-weighted quantum yield ( $\langle\tau\rangle = \sum \alpha_i \tau_i$ ) with the acceptor ( $\langle\tau\rangle_{\text{DA}}$ ) and without the acceptor ( $\langle\tau\rangle_{\text{D0}}$ ).<sup>21</sup> These transfer efficiency values were similar (within 10%) to those determined by fluorescence intensity measurements using a steady-state fluorometer. Because the lifetime measurements are not affected by either a change in donor concentration between samples or inner-filter effects, the transfer efficiencies determined by the lifetime-weighted quantum yield were used here for FRET between AEDANS–Tm and either DAB–F-actin or TNP-ADP–F-actin. In the FRET between probes attached to actin monomers in F-actin, the relation between the transfer efficiency and the acceptor ratio (labeling ratio) depends on the radial coordinates of the donor and acceptor positions in the thin filament. The radial coordinates of Cys374 or Cys10 on F-actin were determined by changing the ratio of the acceptor.<sup>22,23</sup> The FRET measurements using different acceptor labeling ratios give information about the radial coordinates of the donor and the acceptor. Therefore, in order to



**Table 3.** FRET between Tm segment 83–111 and F-actin on the reconstituted thin filament

Tm (D)	$Q_0$ (+Ca), $Q_0$ (–Ca)	Actin (A)	$R_0$ (+Ca), $R_0$ (–Ca)	A/P	$E_{\text{obs}}/E_{\text{calc}}$	
					+Ca <sup>2+</sup>	–Ca <sup>2+</sup>
83 (105%)	0.229, 0.229	DAB	36.5, 36.5	0.5	0.21/0.22	0.21/0.23
				1	0.42/0.39	0.44/0.40
		TNP	37.2, 37.2	0.33	0.21/0.17	0.27/0.18
				0.42	0.27/0.21	0.28/0.23
		FLC	43.2, 43.2	0.56	0.34/0.36	0.35/0.38
90 (87%)	0.256, 0.275	DAB	37.2, 37.6	0.93	0.5/0.51	0.51/0.53
				0.5	0.28/0.23	0.30/0.26
		TNP	37.9, 38.3	1	0.49/0.41	0.53/0.45
				0.33	0.33/0.21	0.38/0.24
		FLC	44.0, 44.6	0.42	0.36/0.26	0.41/0.29
97 (93%)	0.252, 0.271	DAB	37.1, 37.5	0.56	0.37/0.37	0.44/0.40
				0.93	0.54/0.52	0.62/0.55
		TNP	37.8, 38.3	0.5	0.24/0.26	0.26/0.29
				1	0.43/0.48	0.51/0.52
		FLC	43.9, 44.4	0.33	0.34/0.24	0.36/0.26
104 (97%)	0.262, 0.275	DAB	37.3, 37.6	0.42	0.42/0.29	0.44/0.32
				0.56	0.25/0.36	0.25/0.39
		TNP	38.0, 38.4	0.93	0.38/0.49	0.39/0.53
				0.5	0.25/0.26	0.26/0.28
		FLC	44.2, 44.5	1	0.48/0.48	0.51/0.51
111 (93%)	0.242, 0.243	DAB	36.8, 36.8	0.33	0.29/0.24	0.33/0.26
				0.42	0.39/0.29	0.41/0.32
		TNP	37.5, 37.5	0.56	0.27/0.37	0.34/0.40
				0.93	0.38/0.52	0.44/0.55
		FLC	43.6, 43.7	0.5	0.20/0.21	0.20/0.22
				1	0.38/0.39	0.39/0.40
				0.33	0.21/0.21	0.23/0.22
				0.42	0.23/0.26	0.26/0.27
				0.56	0.32/0.38	0.33/0.41
				0.93	0.45/0.54	0.48/0.58

increase the accuracy in locating each Tm segment on F-actin, we measured the transfer efficiencies at different acceptor labeling ratios (two). The  $E_{\text{obs}}$  values are summarized in Tables 1–5.

### Construction of an atomic model for the Tm–F-actin complex on the thin filament

First, we attempted to place the atomic structure of Tm segment 146–174 on the F-actin filament using  $E_{\text{obs}}$  values (Table 1) with and without Ca<sup>2+</sup>. The atomic coordinates for Lorenz *et al.*'s F-actin model (composed of 11 actin monomers) and the Tm crystal structure were used. The C<sup>β</sup> and C<sup>α</sup> coordinates for the labeled amino acid residues in Tm and actin (the O2' atom for TNP-ADP), respectively, were used as the labeled positions. The long axis of F-actin was aligned along the z-axis from the barbed end to the pointed end, and the value of the z-axis was set to zero for the contact surface between the fifth actin monomer and the seventh actin monomer. The x-axis was set along the contact surface between the fifth actin monomer and the sixth actin monomer. Tm segment 146–174 was aligned along the z-axis from its C-terminus to its N-terminus, and the center of the coordinates for the two C<sup>β</sup> atoms of residue 160 in the two Tm chains was placed at Z on the z-axis. The angle between the Tm segment's long

axis and the z-axis was defined as  $\theta$ . The radius of the binding of the Tm segment to actin was defined as  $R$ . The Tm azimuth (angle from the x-axis on an X–Y plane) was defined as  $\phi$ . The rotational angle around the Tm axis was defined as  $\psi$ . Figure 1 shows the five spatial parameters ( $\theta$ ,  $R$ ,  $Z$ ,  $\phi$ , and  $\psi$ ) that describe the Tm segment position on the F-actin filament.

The possible arrangements for the Tm segment on F-actin were explored by systematically changing the values of the five spatial parameters such that all possible orientations were analyzed. The Tm molecule winds along the F-actin filament with a 770-Å pitch, and the length of this segment is ~42 Å. The curvature of this segment on the F-actin filament was estimated to be 19.6°; thus, a straight rod can approximate this segment in the model. Therefore, the atomic coordinates of the Tm segment were used without deforming the shape. At each orientation, the distances between each donor on the two Tm chains and the acceptors on the 11 actin monomers were calculated from the coordinates for each FRET pair. Because transfer efficiency is a function of the inverse of the sixth power of the distance between the donor and the acceptor, calculation with more than five acceptors is unnecessary. The five nearest-neighbor distances (the nearest actin monomer and the four surrounding actin monomers in an F-actin

**Table 4.** FRET between Tm segment 216–244 and F-actin on the reconstituted thin filament

Tm (D)	$Q_0$ (+Ca), $Q_0$ (–Ca)	Actin (A)	$R_0$ (+Ca), $R_0$ (–Ca)	A/P	$E_{\text{obs}}/E_{\text{calc}}$	
					+Ca <sup>2+</sup>	–Ca <sup>2+</sup>
216 (97%)	0.230, 0.228	DAB	36.6, 36.5	0.5	0.21/0.20	0.23/0.21
				1	0.37/0.36	0.40/0.38
		TNP	37.0, 36.9	0.33	0.22/0.24	0.23/0.24
				0.45	0.38/0.31	0.40/0.32
		FLC	43.2, 43.2	0.7	0.36/0.43	0.38/0.46
223 (105%)	0.255, 0.259	DAB	37.1, 37.2	0.82	0.41/0.48	0.42/0.51
				0.5	0.22/0.23	0.22/0.24
		TNP	37.6, 37.7	1	0.44/0.43	0.43/0.45
				0.33	0.31/0.25	0.30/0.26
		FLC	44.0, 44.1	0.45	0.47/0.33	0.47/0.35
230 (89%)	0.261, 0.257	DAB	37.2, 37.2	0.7	0.44/0.45	0.45/0.47
				0.82	0.48/0.49	0.48/0.51
		TNP	37.8, 37.7	0.5	0.19/0.24	0.19/0.25
				1	0.38/0.45	0.39/0.46
		FLC	44.2, 44.0	0.33	0.21/0.24	0.20/0.26
237 (86%)	0.314, 0.316	DAB	38.4, 38.5	0.45	0.30/0.32	0.32/0.34
				0.7	0.39/0.47	0.44/0.48
		TNP	39.0, 39.0	0.82	0.41/0.52	0.45/0.53
				0.5	0.32/0.28	0.32/0.29
		FLC	45.5, 45.6	1	0.58/0.49	0.58/0.50
244 (88%)	0.259, 0.264	DAB	37.2, 37.4	0.33	0.27/0.26	0.31/0.28
				0.47	0.45/0.34	0.45/0.37
		TNP	37.7, 37.9	0.7	0.62/0.53	0.60/0.56
				0.82	0.63/0.58	0.62/0.61
		FLC	44.1, 44.2	0.5	0.22/0.23	0.24/0.24
				1	0.35/0.40	0.40/0.41
				0.45	0.32/0.27	0.37/0.30
				0.47	0.32/0.28	0.38/0.32
				0.7	0.41/0.48	0.47/0.52
				0.82	0.44/0.53	0.51/0.57

filament) were used to calculate the FRET efficiency, as previously analyzed for the FRET between actin monomer probes in an F-actin filament.<sup>22,23</sup> By using these distance values, we calculated the energy transfer efficiency ( $E_{\text{calc}}$ ) for each FRET pair at the acceptor labeling ratio according to Eqs. (2)–(8) in **Materials and Methods**. At each orientation, the squared sum ( $R_{\text{es}}$ ) of deviations of the calculated energy transfer efficiencies from the observed values ( $E_{\text{obs}}$ ) for all FRET pairs was calculated as follows:

$$R_{\text{es}} = \sum_{\text{data set}} (E_{\text{obs}} - E_{\text{calc}})^2 \quad (1)$$

At the fixed values of  $R$ ,  $\theta$ ,  $Z$ , and  $\phi$  (initial values),  $\psi$  was changed from  $0^\circ$  to  $360^\circ$  with a step size of  $5^\circ$ , and the minimum value of the residuals was obtained. Next,  $\phi$  was changed from  $0^\circ$  to  $180^\circ$  with a step size of  $2^\circ$ . At each  $\phi$  value,  $\psi$  was changed from  $0^\circ$  to  $360^\circ$  with a step size of  $5^\circ$ , and the minimum value of the residuals was obtained.  $Z$  was then changed from  $-28 \text{ \AA}$  to  $28 \text{ \AA}$  with a step size of  $1 \text{ \AA}$ . At each  $Z$  value, the  $\phi$  and  $\psi$  values were changed as described above such that the minimum value of the residuals was obtained.  $\theta$  was changed from  $-4^\circ$  to  $-32^\circ$  with a step size of  $1^\circ$ . At each  $\theta$  value, the  $Z$ ,  $\phi$ , and  $\psi$  values were systematically changed at the fixed value of  $R$ . Finally,  $R$  was changed from  $36 \text{ \AA}$  to  $45 \text{ \AA}$  with a step size of  $1 \text{ \AA}$ . At

each  $R$  value, the  $\theta$ ,  $Z$ ,  $\phi$ , and  $\psi$  values were systematically changed. Thus, the global minimum of residuals was obtained.

First, we searched for the orientation of the Tm segment using the 30 FRET efficiencies observed with  $\text{Ca}^{2+}$  (Table 1). By changing  $\psi$  from  $0^\circ$  to  $360^\circ$ ,  $\phi$  from  $0^\circ$  to  $180^\circ$ , and  $Z$  from  $-28 \text{ \AA}$  to  $+28 \text{ \AA}$  at constant  $R$  and  $\theta$  values, we determined the minimum values of the residuals for each  $\phi$  and  $Z$  value. A three-dimensional map of the residuals as a function of  $\phi$  and  $Z$ , at constant  $R$  and  $\theta$  values, is shown in Fig. S3. By changing  $R$  from  $36 \text{ \AA}$  to  $44 \text{ \AA}$  and  $\theta$  from  $-4^\circ$  to  $-24^\circ$ , we determined the minimum values of the residuals for each  $R$  and  $\theta$  value. The three-dimensional map of the residuals as a function of  $R$  and  $\theta$  is shown in Fig. S4. The results show a distinct minimum value of the residuals for each of the five spatial parameters.

The global minimum of the residuals was obtained at  $R=41 \text{ \AA}$ ,  $\theta=-21^\circ$ ,  $Z=+7 \text{ \AA}$ ,  $\phi=40^\circ$ , and  $\psi=345^\circ$ . By using the FRET efficiencies obtained without  $\text{Ca}^{2+}$ , we searched for the orientation of the Tm segment using the same procedure described for Tm with  $\text{Ca}^{2+}$ . The results also showed a distinct minimum value of the residuals for each spatial parameter (Figs. S3 and S4). The global minimum of the residuals was obtained at  $R=40 \text{ \AA}$ ,  $\theta=-17^\circ$ ,  $Z=+4 \text{ \AA}$ ,  $\phi=38^\circ$ , and



**Table 5.** FRET between Tm segment 251–279 and F-actin on the reconstituted thin filament

Tm (D)	$Q_0$ (+Ca), $Q_0$ (–Ca)	Actin (A)	$R_0$ (+Ca), $R_0$ (–Ca)	A/P	$E_{\text{obs}}/E_{\text{calc}}$	
					+Ca <sup>2+</sup>	–Ca <sup>2+</sup>
252 (100%)	0.285, 0.275	DAB	36.6, 36.5	0.5	0.29/0.26	0.28/0.27
				1	0.48/0.45	0.50/0.46
		TNP	37.0, 36.9	0.45	0.43/0.34	0.45/0.33
				0.61	0.47/0.43	0.50/0.42
		FLC	43.2, 43.2	0.51	0.37/0.41	0.37/0.43
258 (88%)	0.252, 0.263	DAB	37.1, 37.2	0.88	0.48/0.58	0.50/0.61
				0.5	0.26/0.24	0.20/0.25
		TNP	37.6, 37.7	1	0.42/0.43	0.41/0.44
				0.45	0.34/0.32	0.36/0.33
		FLC	44.0, 44.1	0.61	0.41/0.43	0.39/0.44
265 (101%)	0.251, 0.246	DAB	37.2, 37.2	0.51	0.34/0.37	0.34/0.40
				0.88	0.48/0.53	0.50/0.57
		TNP	37.8, 37.7	0.5	0.24/0.27	0.25/0.27
				1	0.40/0.49	0.42/0.49
		FLC	44.2, 44.0	0.45	0.34/0.34	0.33/0.36
272 (100%)	0.298, 0.299	DAB	37.2, 37.4	0.61	0.36/0.45	0.40/0.46
				0.51	0.32/0.37	0.34/0.39
		TNP	39.0, 39.0	0.88	0.47/0.53	0.52/0.54
				0.5	0.30/0.30	0.30/0.31
		FLC	45.5, 45.6	1	0.58/0.53	0.61/0.55
279 (97%)	0.294, 0.300	DAB	37.2, 37.4	0.45	0.41/0.37	0.43/0.39
				0.61	0.42/0.47	0.42/0.50
		TNP	37.7, 37.9	0.51	0.49/0.44	0.49/0.45
				0.88	0.66/0.60	0.66/0.61
		FLC	44.1, 44.2	0.5	0.27/0.27	0.29/0.28
				1	0.51/0.46	0.54/0.49
				0.45	0.45/0.34	0.52/0.38
				0.61	0.52/0.43	0.56/0.48
				0.51	0.42/0.45	0.48/0.47
				0.88	0.58/0.62	0.64/0.65

$\psi=355^\circ$ . The root-mean-square errors between the calculated transfer efficiencies and the observed values were 0.059 and 0.070 with and without Ca<sup>2+</sup>, respectively. Comparisons of the individual FRET efficiencies calculated for the best-fit models of the observed data, which indicate a good fit, are shown in Table 1.

Using the same procedures, we searched for the orientation of Tm segment 41–69 on the F-actin filament. The global minimum of the residuals was obtained at  $R=42$  Å,  $\theta=-6^\circ$ ,  $Z=-14$  Å,  $\phi=28^\circ$ , and  $\psi=170^\circ$  for the +Ca<sup>2+</sup> state, with a root-mean-square error of 0.062. The minimum was obtained at  $R=40$  Å,  $\theta=-12^\circ$ ,  $Z=-11$  Å,  $\phi=32^\circ$ , and  $\psi=210^\circ$  for the –Ca<sup>2+</sup> state, with a root-mean-square error of 0.054. Comparisons of the individual FRET efficiencies for the best-fit models of the observed data are presented in Table 2.

For Tm segment 83–111, the global minimum of the residuals was obtained at  $R=43$  Å,  $\theta=-10^\circ$ ,  $Z=-17$  Å,  $\phi=26^\circ$ , and  $\psi=245^\circ$  for the +Ca<sup>2+</sup> state, with a root-mean-square error of 0.069. The minimum was obtained at  $R=42$  Å,  $\theta=-9^\circ$ ,  $Z=-20$  Å,  $\phi=24^\circ$ , and  $\psi=245^\circ$  for the –Ca<sup>2+</sup> state, with a root-mean-square error of 0.073. Comparisons of the individual FRET efficiencies for the best-fit models of the observed data are presented in Table 3.

For Tm segment 216–244, the global minimum of the residuals was obtained at  $R=41$  Å,  $\theta=-28^\circ$ ,  $Z=21$  Å,  $\phi=48^\circ$ , and  $\psi=10^\circ$  for the +Ca<sup>2+</sup> state, with a root-mean-square error of 0.063. The minimum was obtained at  $R=40$  Å,  $\theta=-23^\circ$ ,  $Z=23$  Å,  $\phi=50^\circ$ , and  $\psi=10^\circ$  for the –Ca<sup>2+</sup> state, with a root-mean-square error of 0.055. Comparisons of the individual FRET efficiencies for the best-fit models of the observed data are presented in Table 4.

For Tm segment 251–279, the global minimum of the residuals was obtained at  $R=40$  Å,  $\theta=-15^\circ$ ,  $Z=-27$  Å,  $\phi=22^\circ$ , and  $\psi=65^\circ$  for the +Ca<sup>2+</sup> state, with a root-mean-square error of 0.055. The minimum was obtained at  $R=39$  Å,  $\theta=-12^\circ$ ,  $Z=-24$  Å,  $\phi=24^\circ$ , and  $\psi=70^\circ$  for the –Ca<sup>2+</sup> state, with a root-mean-square error of 0.061. Comparisons of the individual FRET efficiencies for the best-fit models of the observed data are presented in Table 5.

These segments were arranged on an F-actin filament such that segment 41–69 was moved by +6 actin monomers ( $-166.154^\circ \times \pi/180^\circ \times 6$  rotations and +27.5 Å  $\times 6$  transitions), segment 83–111 was moved by +4 actin monomers, segment 216–244 was moved by –4 actin monomers, and segment 251–279 was moved by –6 actin monomers. Figure 2 shows the stereo views for the best-

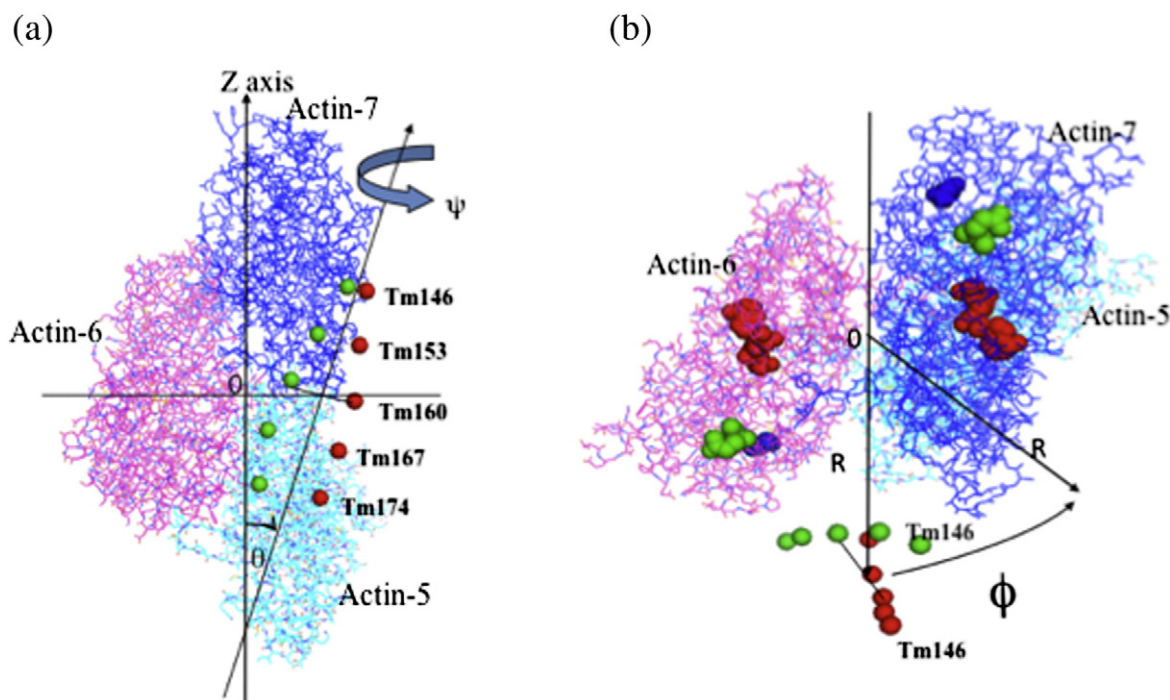


**Fig. 1.** Tm segment 146–174 was positioned on F-actin, with the five spatial parameters used to search for all possible orientations. For the calculations, the coordinates of the 11 actin monomers were used, although only the fifth actin monomer up to the seventh actin monomer are shown here. (a) View along the F-actin axis. The red and green spheres show the  $\alpha$ -carbon atoms of the donor-labeled residues in two  $\alpha$ -chains of Tm. (b) View from the pointed end. Cys374, Gln41, and bound ADP on the sixth and seventh actin monomers are shown in blue, green, and red spheres, respectively.

fit models of F-actin and these Tm segments with and without  $\text{Ca}^{2+}$ .

## Discussion

In the FRET analysis, due to the ambiguity in the value of the dipole–dipole orientation factor between energy donor molecules and energy acceptor molecules and due to the dimensions of the probes attached by linkers to the side chains of the amino acid residues, the measured distance will have an uncertainty of  $\pm 10\%$ .<sup>14</sup> Although the length of probe linkers is  $\sim 10$  Å, the linker does not extend towards unidirection but folds randomly. In the case of two donors and multiple acceptors, as in the present FRET experiments, the directions of the linker's extension would be further randomized. Using the observed intramonomer and intermonomer FRET efficiencies of actin, we constructed a FRET model of the actin monomer and oriented the actin monomer within a filament. In spite of the uncertainty derived from the orientation factor and the probe size, the FRET model was in good agreement with the atomic model of G-actin and the actin filament.<sup>24</sup> For many different proteins and peptides, there is accumulating evidence supporting the notion that FRET distances indeed

reflect the nearly equivalent distances determined by crystallography.<sup>14</sup> Since the atomic coordinates of the amino acid residues of proteins, but not of probes, are available in the present model construction, we cannot directly evaluate the ambiguity derived from the linkers' lengths. In rigid-body movement calculation, instead of the  $\text{C}^\beta$  coordinates, the  $\text{C}^\alpha$  and  $\text{C}^\gamma$  coordinates of the labeled amino acid residues on Tm were used as label positions, but the best-fit models were almost the same. The use of the  $\text{C}^\beta$  coordinates yielded a better fit (smaller root-mean-square errors) in the calculation. This suggests that small deviations in the probe from the  $\text{C}^\beta$  positions of the attached amino acid residues do not alter the model significantly. Despite such difficulties in analysis, FRET methods have many advantages compared with other biophysical methods: provision of information about the thin filament structure in the physiological solution and absence of need to orient the filament direction uniformly. Furthermore, energy donor and energy acceptor probes are specifically attached to proteins, so that assigning a vector to conformational change is obvious. Using 30 FRET efficiencies (5 donors  $\times$  3 acceptors  $\times$  2 labeling ratios) as restraints, we determined the location for each Tm segment on the F-actin filament with or without  $\text{Ca}^{2+}$ . Here we evaluate the models by

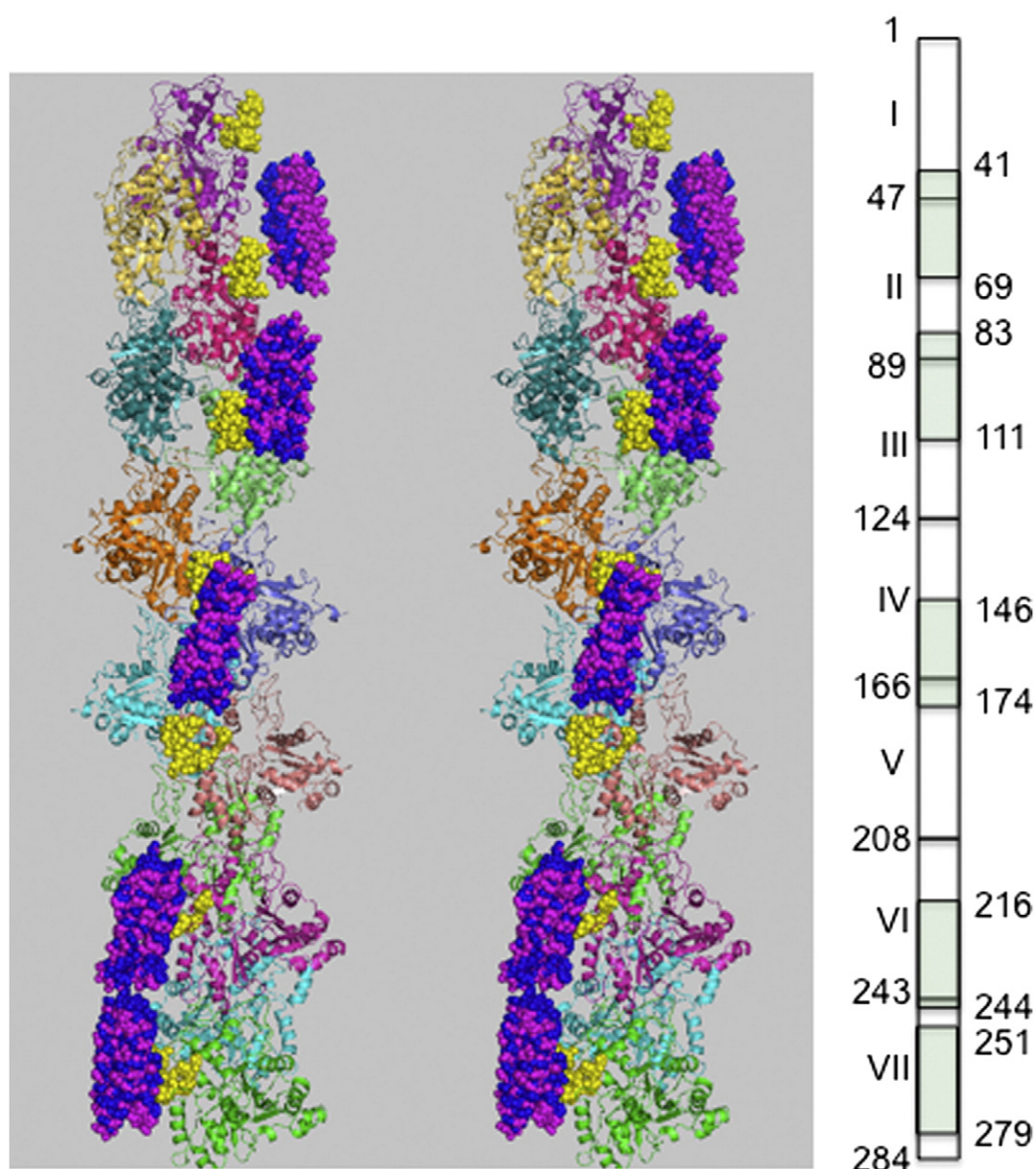


**Fig. 2.** Stereo views of the best-fit models for the five Tm segments and the F-actin complex. Tm has seven quasi-equivalent periods. The Tm segments are shown in magenta and blue with and without  $\text{Ca}^{2+}$ , respectively. The Tm binding region (217–236) proposed by Flaherty *et al.*<sup>25</sup> is represented by yellow spheres.

comparing them with other biochemical and structural studies on Tm and the thin filament.

Flaherty *et al.* suggested the involvement of the Cys217-Leu236 actin region in the Tm interaction.<sup>25</sup> Figure 2 shows that the Tm molecule runs along these residues on an F-actin filament. Tm contains seven quasi-equivalent periods and spans seven actin monomers. Segment 41–69 is located at period 1 (41–46) and period 2 (47–69); segment 83–111 is located at period 2 (83–88) and period 3 (89–111); segment 146–174 is located at period 4 (146–165) and period 5 (166–174); segment 216–244 is located at

period 6 (216–242) and period 7 (243, 244); and segment 251–279 is located at period 7 (243, 244); and segment 251–279 is located at period 7. Figure 2 shows the junction between these Tm periods at the contact region between actin monomers along the long-pitch helix of F-actin, which indicates that each Tm period covers an actin monomer. The 3D-EM analysis of the reconstituted thin filament<sup>26</sup> generated a slightly smaller radius of 38 Å, but neutron scattering experiments<sup>27</sup> and X-ray scattering analysis<sup>11</sup> generated radii of 38–41 Å and 40–42 Å, respectively. The radial values in the best-fit model are similar to these. There is reasonable agreement in



the literature that the radius of the binding of Tm to actin does not significantly change in response to  $\text{Ca}^{2+}$  binding.<sup>27</sup> For the model herein, the radii changed slightly (by 1–2 Å).

Although Tm has seven quasi-equivalent periods, no precise homology was observed in the Tm polypeptide chain; thus, Tm does not necessarily interact with the seven actin monomers in an equivalent manner. In the best-fit model, each segment has a different binding radius and a different angle  $\theta$  between the F-actin long axes and the Tm segment, demonstrating that Tm does not uniformly wind around the F-actin filament.

Figure 3 provides detailed stereo views of the contact surfaces between actin and Tm segment (41–69) with and without  $\text{Ca}^{2+}$ , which are shown using spheres for the actin and Tm residue side chains

within 10 Å of each other. In the  $+\text{Ca}^{2+}$  model, Asp55(T) is close to Lys238. Here, Asp55(T) and Lys238 denote Asp55 on Tm and Lys238 on actin, respectively. Lys59(T) is close to Glu237. Glu62(T) is close enough to Ser235 to form a hydrogen bond. Lys65(T) is possibly close enough to Thr229 to form a hydrogen bond by moving the direction of its long side chain. The directions of the side chains of amino acid residues determined in the crystal structure are not fixed but very mobile under physiological conditions. Glu69(T) is close to Thr229. In the  $-\text{Ca}^{2+}$  model, Asp41(T) is close to Lys315. Lys48(T) is close to Thr318 and Ser323. Lys49(T) is close to Ser323. Since lysine has a long and flexible side chain, the above pairs may become close enough to form a hydrogen bond by moving the side-chain direction. Lys59(T) is close to Ser235 and Glu237.

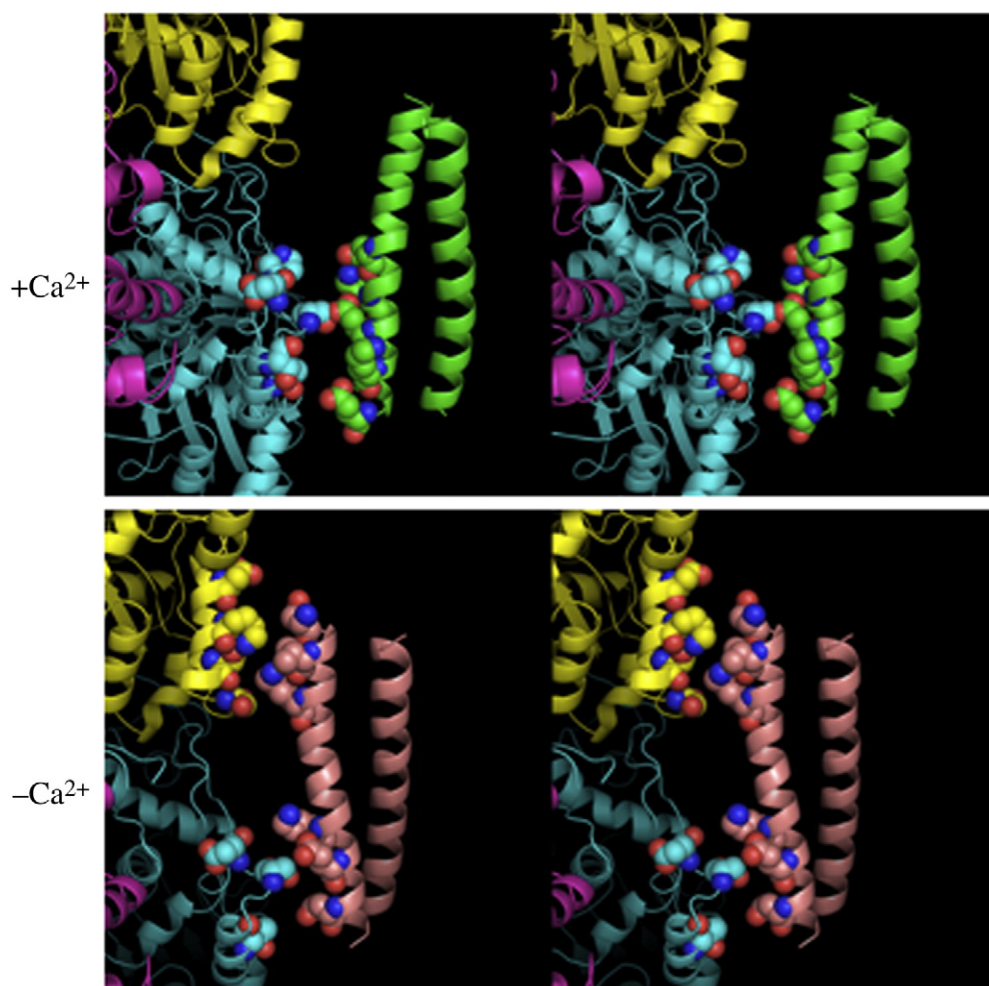


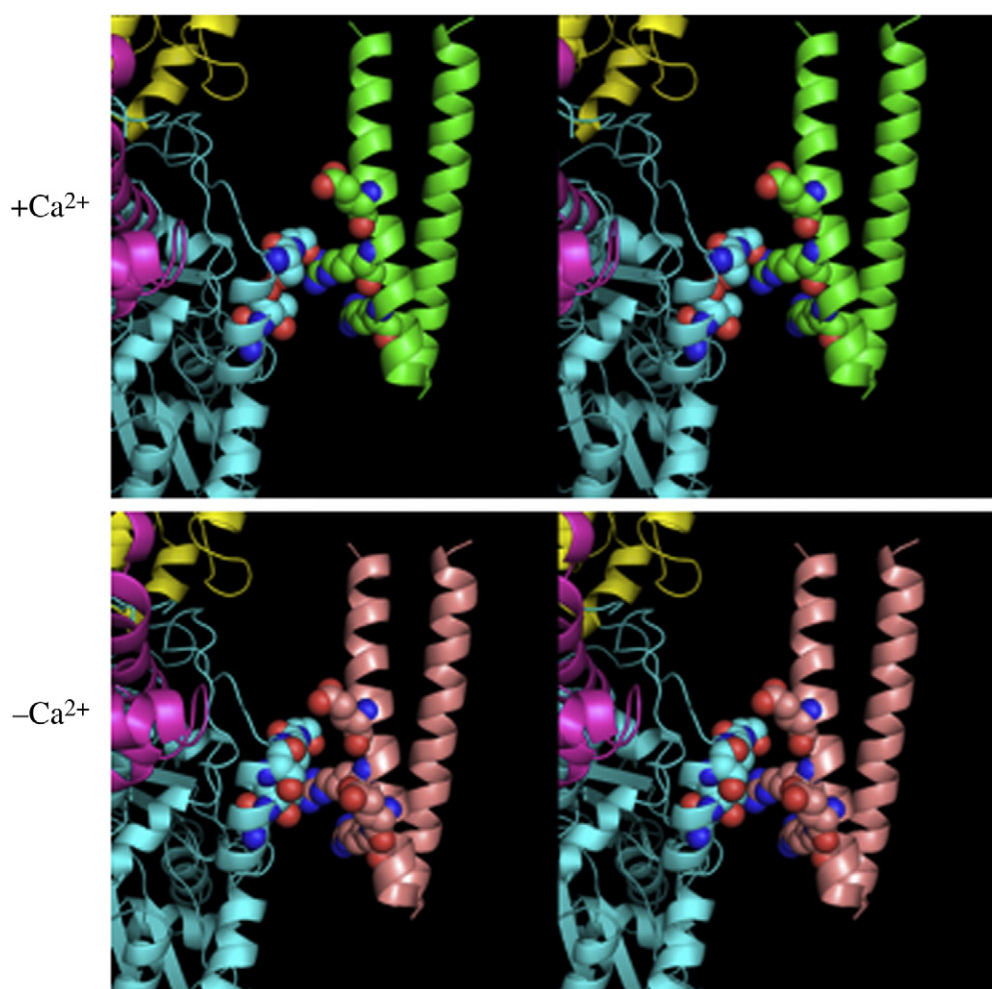
**Fig. 3.** A detailed view of the contact surface between F-actin and Tm (41–69) with  $\text{Ca}^{2+}$  (top) and without  $\text{Ca}^{2+}$  (bottom). +Ca: Actins Thr229, Ser232, Ser235, Glu237, and Lys238, as well as Asp55, Lys59, Glu62, Lys65, and Glu69 on one chain of Tm, are represented by spheres. The red and blue spheres show oxygen and nitrogen atoms, respectively. –Ca: Actins Ser233, Ser235, Glu237, Lys315, Thr318, and Ser323, as well as Asp41, Lys48, Lys49, Lys59, Glu62, and Asp66 on one chain of Tm, are represented by spheres.

Glu62(T) is close to Ser235. Asp66(T) is close to Ser233 and Ser235.

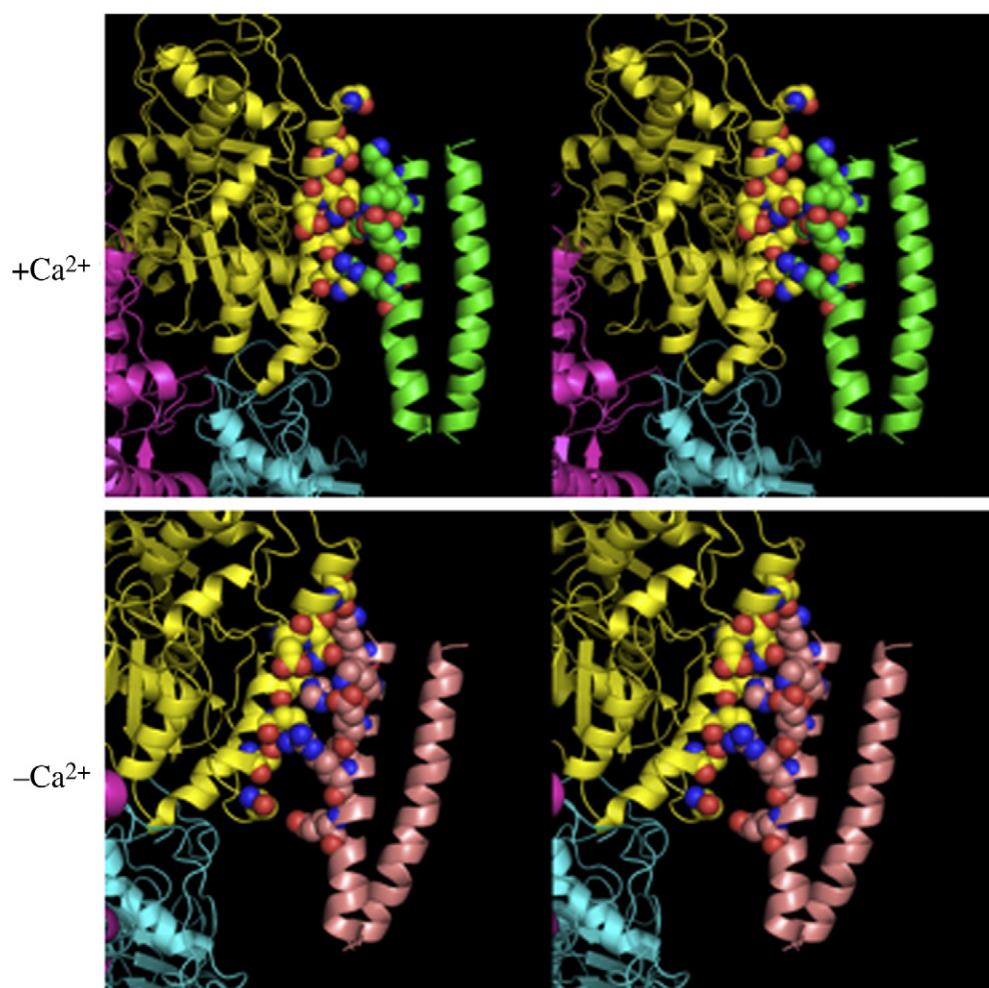
Figure 4 provides detailed stereo views of the contact surfaces between actin and Tm segment (83–111). In the  $+Ca^{2+}$  model, Glu97(T) is close to Ser235. Arg101(T) is close to Thr229 and Ser234, and close enough to Ser235 to form a hydrogen bond. Arg105(T) is close to Glu226 and Thr229, and may possibly form a hydrogen bond with Thr229 by moving the side-chain direction. In the  $-Ca^{2+}$  model, Glu97(T) is close to Ser234 and Ser235, and may possibly form a hydrogen bond with Ser235 by moving the side-chain direction. Arg101(T) is close to Thr229, Ser232, Ser234, and Ser235, and may possibly form a hydrogen bond with Thr229. Glu104(T) is close to Ser232. Arg105(T) is close to Glu226 and Asn225.

Figure 5 provides detailed stereo views of the contact surfaces between actin and Tm segment (146–174). In the  $+Ca^{2+}$  model, Lys149(T) is close to

Glu226, Thr229, and Ser235, and may possibly form a hydrogen bond with Thr229 by moving the side-chain direction. Lys152(T) is close enough to Asn225 and Asp222 to form a hydrogen bond and an ionic bridge. His153(T) is close to Asp222 and Asp311, and contacts the side chain of Lue221. Glu156(T) is possibly close enough to Asn225 to form a hydrogen bond. While Asp157(T) is close to Lys315, Arg160(T) is close to Lys315 and Glu224. Then, it is probable for Asp157(T) and Arg160(T) to form an ionic bridge with Lys315 and Glu224, respectively. In the  $-Ca^{2+}$  model, Lys149(T) is close to Leu221, Glu226, and Thr229, and may possibly form a hydrogen bond with Thr229. Lys152(T) is fairly close to Asn225 to form a hydrogen bond. His153(T) is close to Glu224 and Asp311 to form an ionic bridge. Glu156(T), Asp157(T), and Arg160(T) are close to Lys315. Glu164(T) is close to Ser323 ( $\sim 7$  Å) but not close enough to form a hydrogen bond.



**Fig. 4.** A detailed view of the contact surface between F-actin and Tm (83–111) with  $Ca^{2+}$  (top) and without  $Ca^{2+}$  (bottom).  $+Ca$ : Actins Glu226, Thr229, Ser234, and Ser235, as well as Glu97, Arg101, and Arg105 on one chain of Tm, are represented by spheres.  $-Ca$ : Actins Asn225, Glu226, Thr229, Ser232, Ser234, and Ser235, as well as Glu97, Arg101, Glu104, and Arg105 on one chain of Tm, are represented by spheres.



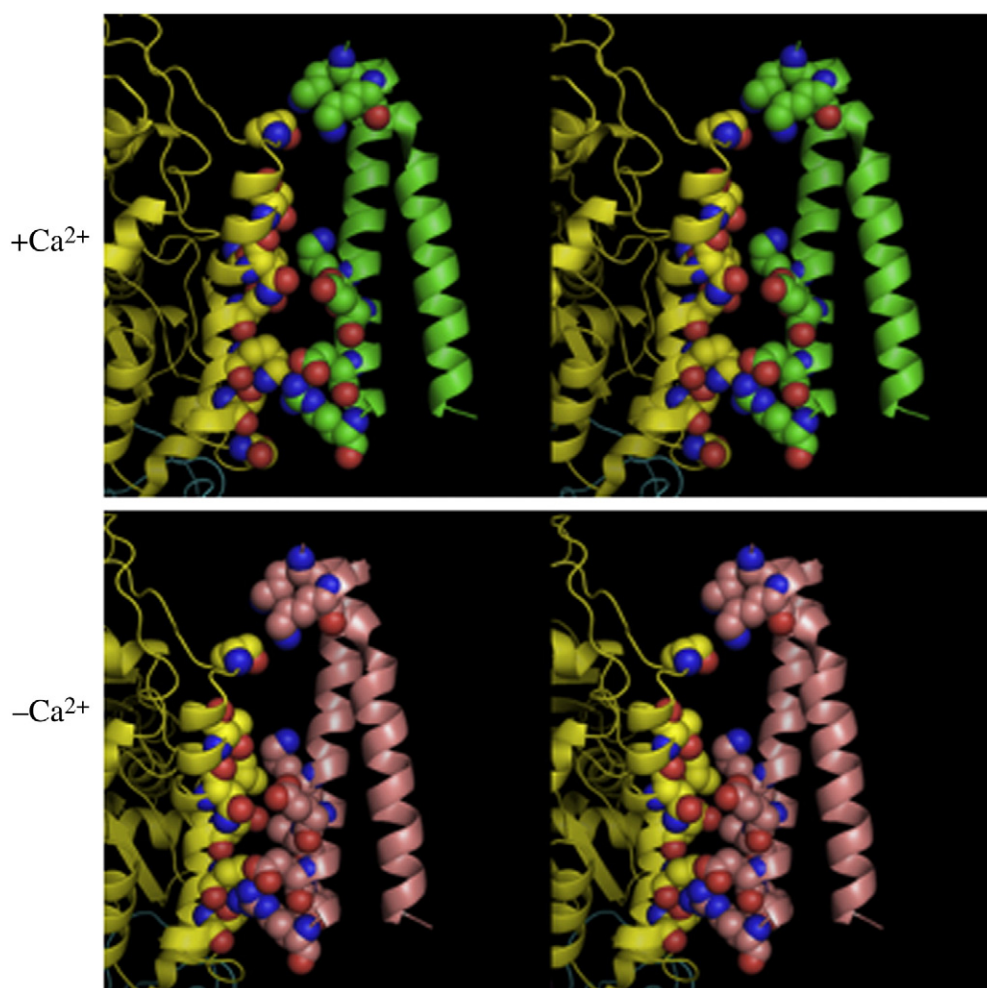
**Fig. 5.** A detailed view of the contact surface between F-actin and Tm (146–174) with  $\text{Ca}^{2+}$  (top) and without  $\text{Ca}^{2+}$  (bottom). +Ca: Actins Leu221, Asp222, Glu224, Asn225, Glu226, Thr229, Ser235, Asp311, and Lys315, as well as Lys149, Lys152, His153, Glu156, Asp157, and Arg160 on one chain of Tm, are represented by spheres. –Ca: Actins Leu221, Glu224, Asn225, Glu226, Thr229, Asp311, Lys315, and Ser323, as well as Lys149, Lys152, His153, Glu156, Asp157, Arg160, and Glu164 on one chain of Tm, are represented by spheres.

Figure 6 provides detailed stereo views of the contact surfaces between actin and Tm segment (216–244). In the  $+\text{Ca}^{2+}$  model, Lys217(T) is close to Ser235, but Lys220(T) is closer to Ser235 to form a hydrogen bond. Lys233(T) is close enough to Leu221 and Asp311 to form a hydrophobic interaction and an ionic bridge by moving the long side chain. Glu236(T) is close to Asn225. Glu240(T) is close enough to Lys315 to form an ionic bridge by changing the side-chain direction of Lys315. Arg244(T) is close to Thr318 ( $\sim 7$  Å) or Ser323 ( $\sim 9$  Å) but possibly closer enough to form a hydrogen bond ( $\sim 3$  Å) by moving the long side chain. In the  $-\text{Ca}^{2+}$  model, Lys217(T) is close to Ser235. Lys220 is possibly close enough to Ser235 to form a hydrogen bond. Lys233(T) is very close to Leu221 to form a hydrophobic interaction. Glu236(T) is possibly close enough to Asn225 to form a

hydrogen bond. Glu240(T) is close enough to Lys315 to form an ionic bridge. Arg244 is close to Lys315 but could move fairly close to Thr318 and Ser323 to form hydrogen bonds.

Figure 7 provides detailed stereo views of the contact surfaces between actin and Tm segment (252–279). In the  $+\text{Ca}^{2+}$  model, Lys264(T) is in contact with Ser235. Lys268(T) is close enough to Thr229 to form a hydrogen bond. Glu272 is in contact with Leu221 to form a hydrophobic interaction. Asp275(T) is possibly close enough to Asn225 to form a hydrogen bond. His276(T) is close to Asp311. Asp279(T) is possibly close enough to Lys315 to form a hydrogen bond. In the  $-\text{Ca}^{2+}$  model, Lys264(T) is close enough to Ser235 to form a hydrogen bond. Lys268 is possibly close enough to Thr229 to form a hydrogen bond. Glu272(T) is possibly in contact with Leu221. Asp275(T) is





**Fig. 6.** A detailed view of the contact surface between F-actin and Tm (216–244) with  $\text{Ca}^{2+}$  (top) and without  $\text{Ca}^{2+}$  (bottom). +Ca: Actins Leu221, Asn225, Ser235, Asp311, Lys315, Thr318, and Ser323, as well as Lys217, Lys220, Lys233, Glu236, Glu240, and Arg244 on one chain of Tm, are represented by spheres. –Ca: Actins Leu221, Asn225, Thr229, Ser235, Asp311, Thr318, Lys315, and Ser323, as well as Lys217, Lys220, Lys233, Glu236, Glu240, and Arg244 on one chain of Tm, are represented by spheres.

possibly close enough to Asn225 to form a hydrogen bond. His276(T) is in contact with Asp311. Asp279 (T) is close enough to Lys315 to form an ionic bridge.

Figures 3–7 show that the C-terminal region of Tm contacts actin more closely than does the N-terminal region. For these five segments, actins Leu221(3), Asp222(1), Glu224(1), Asn225(3), Glu226(2), Thr229 (4), Ser232(1), Ser234(1), Ser235(5), Asp311(3), Glu237(1), Lys238(1), Lys315(3), Thr318(1), and Ser323(1) are close to the ionic residues in Tm in the presence of  $\text{Ca}^{2+}$ . Actins Leu221(3), Glu224(1), Asn225(4), Glu226(2), Thr229(4), Ser232(1), Ser233 (1), Ser234(1), Ser235(4), Glu237(1), Asp311(3), Lys315(4), Thr318(2), and Ser323(3) are close to the ionic residues in Tm in the absence of  $\text{Ca}^{2+}$  (the number in parentheses shows the frequency of the five Tm segments). The model herein indicates that actins Leu221, Asn225, Thr229, Ser235, Asp311,

Lys315, and Ser323 are important for Tm binding because these residues form multiple interactions with the Tm residues. It is widely believed that ionic forces have an important role in the actin–Tm interaction. In the model herein, not all but many of the ionic amino Tm residues shown by spheres in Figs. 3–7 are sufficiently close to either ionic or hydrophilic actin residues to form either ionic bridges or hydrogen bonds. If the Tm helix structure fluctuates considerably and if the Tm position on F-actin fluctuates by several angstroms under physiological conditions, more residues could become close enough to actin residues to form a hydrogen bond or an ionic bridge. That actin Leu221 is at the contact site suggests that not only ionic interactions and hydrogen bonding in Tm binding but also hydrophobic interactions are involved. Using site-directed mutagenesis, Saeki *et al.*<sup>28</sup> replaced the

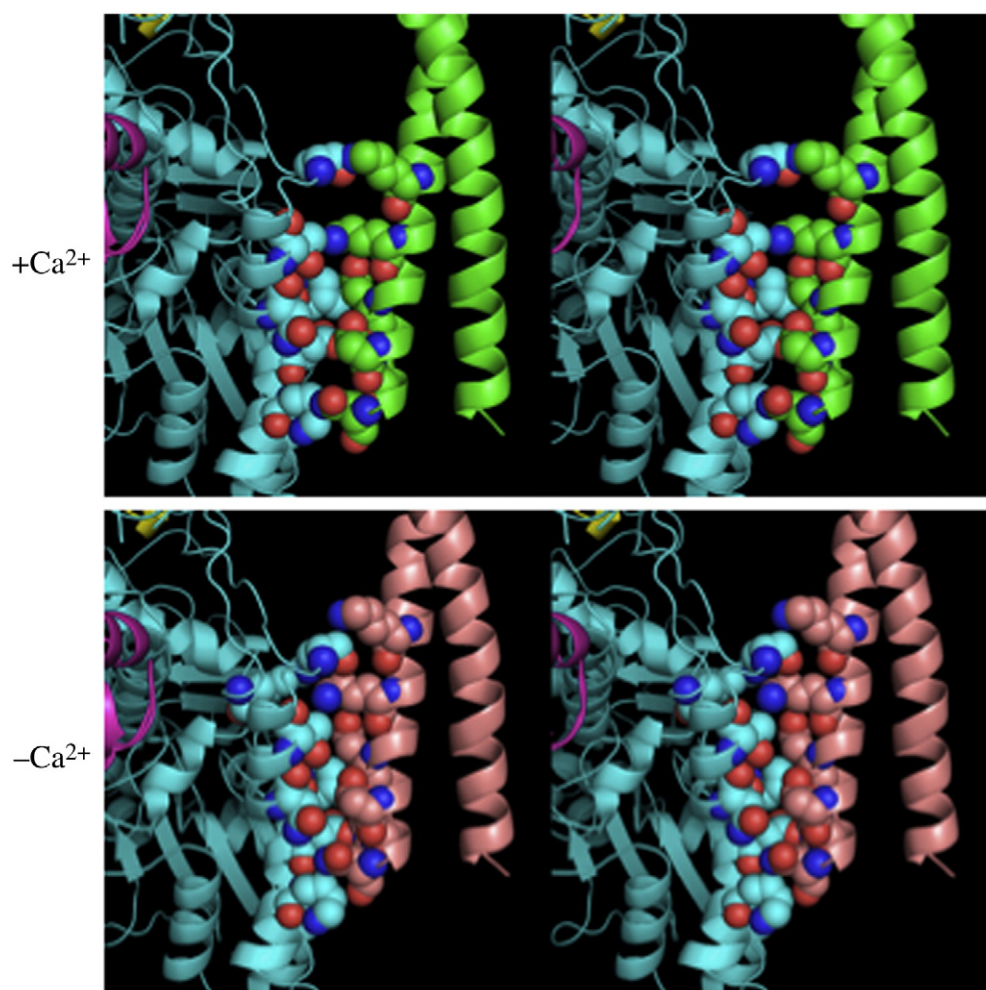


**Fig. 7.** A detailed view of the contact surface between F-actin and Tm (251–279) with  $\text{Ca}^{2+}$  (top) and without  $\text{Ca}^{2+}$  (bottom). +Ca: Actins Leu221, Asn225, Thr229, Ser235, Asp311, and Lys315, as well as Lys264, Lys268, Glu272, Asp275, His276, and Asn279 on one chain of Tm, are represented by spheres. –Ca: Actins Leu221, Asn225, Thr229, Ser235, Asp311, and Lys315 on actin, as well as Lys264, Lys268, Glu272, Asp275, His276, and Asn279 on one chain of Tm, are represented by spheres.

*Dictyostelium* actin sequence 228–232 (QTAAS) with (KAYKE) from *Tetrahymena* actin that does not bind Tm.<sup>29</sup> The resulting *Dictyostelium*/*Tetrahymena* chimeric actin did not bind Tm without Tn. They concluded that residues 228–232 are found in the Tm binding site. Asn225 and Thr229 in rabbit skeletal muscle actin are replaced with Ala in *Tetrahymena* actin, which cannot form hydrogen bonds and results in the inability to bind Tm. Furthermore, the best-fit model shows that actin Thr229 is often close to basic Tm residues, suggesting that replacement of Q228 with Lys228 in *Dictyostelium* actin significantly impairs Tm binding, as demonstrated by Saeki and Wakabayashi.<sup>30</sup>

Based on 3D-EM reconstruction and computational chemistry, an atomic model of Tm–F-actin has been constructed.<sup>31</sup> The clusters of basic amino acids on actin subdomains 1 and 3 juxtaposed against acidic residues on the successive quasi-repeating

units of Tm were used for modeling. We identified the actin and Tm residues that closely contact each other, which are different from the residues identified in our present model. While 3D-EM showed that Tm runs on actin subdomains 1 and 3 along the filament, the present model showed that Tm runs on actin subdomains 3 and 4. Therefore, there is a large discrepancy between actin residues close to Tm that were determined by 3D-EM and actin residues close to Tm that were determined by three-dimensional FRET analysis. It should be noted here that the actin–Tm interaction involves hydrogen bonds, since Tm dissociates from F-actin at elevated temperature.<sup>32</sup> The present model shows many hydrogen-bond formations between actin and Tm.

The 3D-EM experiment using a reconstituted thin filament has been used to visualize  $\text{Ca}^{2+}$ -induced Tm movement. Numerous reports have shown that the Tm strand moves azimuthally by either  $\sim 25^\circ$  or

15–20° (Milligan and Flicker,<sup>9</sup> Lehman *et al.*,<sup>10</sup> Narita *et al.*,<sup>11</sup> and Poole *et al.*,<sup>12</sup> see reviews by Perry<sup>2</sup> and Squire and Morris<sup>13</sup>). However, no significant  $\text{Ca}^{2+}$ -induced change in the transfer efficiency has been detected.<sup>15–19</sup> Despite these data, using fluorescence lifetime analysis, Bacchiocchi and Lehrer reported that Tm undergoes a  $\text{Ca}^{2+}$ -induced 17° azimuthal shift with respect to actin on the filament.<sup>17</sup> Their FRET measurements detected no significant change in the transfer efficiency between AEDANS attached to Tm Cys190 and tetramethylrhodamine–phalloidin bound to F-actin. As the FRET experiments for labels attached to actin and Tm include a complicated multiple donor–acceptor system, the donor lifetime should have many decay components. Typically, multi-exponential decay is difficult to resolve.<sup>21</sup> Therefore, it is hard to obtain a meaningful analysis from single-shot lifetime measurements. With analysis of one FRET pair, it might be possible to find two azimuthally different positions and orientations for Tm on an F-actin filament that have almost the same transfer efficiency. However, it is impossible to find two such azimuthally different Tm positions by analyzing many FRET pairs simultaneously. The transfer efficiencies for the 30 different FRET pairs measured herein are particularly sensitive to the azimuth angle  $\phi$  (Fig. S3). Given the small  $\text{Ca}^{2+}$ -induced change in the transfer efficiencies, the  $\text{Ca}^{2+}$ -induced azimuthal shift should be small, as shown in Fig. 2. However, the contact surface between actin and Tm significantly changes (Figs. 3–7). The values  $R$ ,  $\theta$ , and  $\psi$  differ substantially between the  $+\text{Ca}^{2+}$  state and the  $-\text{Ca}^{2+}$  state. This spatial rearrangement results in several angstroms of translational movements of the residues implicated in the actin–Tm interaction, which could induce a significant conformational change in F-actin through the seven Tm regions. Figures 3–7 show that Tm binds actin with more residues in the  $-\text{Ca}^{2+}$  state than in the  $+\text{Ca}^{2+}$  state. The model also shows that the Tm helices run along actin helices 309–320 and 223–230 in subdomains 2 and 3, respectively (Fig. S5). Saeki and Wakabayashi produced a mutant A230Y in *Dictyostelium* actin, which bound Tm normally and had an approximately 5-fold higher  $\text{Ca}^{2+}$  activation with Tm and Tn compared with wild-type actin.<sup>30</sup> Actin residue 230 is located in helix 223–230 at the opposite side from the Tm binding surface and is distal to the myosin binding site. The results suggest that a conformational change near the Tm binding site but far from the myosin binding site alters thin filament cooperativity and can regulate actomyosin ATPase activity. Although there is no significant  $\text{Ca}^{2+}$ -induced azimuthal shift, the  $\text{Ca}^{2+}$ -induced changes in the actin–Tm contact surface may induce a significant conformational change in the F-actin structure, which would be important for muscle regulation. Tm may control the actin filament structure through interac-

tions with helices 309–320 and 223–230 on the actin monomer.

In conclusion, a three-dimensional FRET analysis with 30 FRET efficiencies was used to determine the location of a Tm segment on an actin filament. This model is consistent with previous biochemical and structural studies on Tm and the thin filament, except for the  $\text{Ca}^{2+}$ -induced azimuthal Tm shift that was derived from 3D-EM and X-ray scattering analyses. To resolve this discrepancy, we need to construct atomic models of F-actin and the Tm–Tn complex, which would reveal the regulation mechanism for striated muscle contraction.

## Materials and Methods

### Reagents

*Amanita phalloides* phalloidin was purchased from Sigma. IAEDANS and DABMI were purchased from Molecular Probes. TNP-ATP was synthesized according to the method described by Hiratsuka.<sup>33</sup> The microbial transglutaminase was a gift from Ajinomoto Co. All other chemicals were of analytical grade.

### Protein preparations

Actin, S1, and Tn were prepared from rabbit skeletal muscle using the procedures of Spudich and Watt,<sup>34</sup> Weeds and Taylor,<sup>35</sup> and Ebashi *et al.*,<sup>36</sup> respectively. Rabbit  $\alpha$ -Tm was prepared from rabbit cardiac muscle.<sup>18</sup> To prepare the single-cysteine Tm mutants, we began with AAS- $\alpha$ -TmC190I cDNA, which had a tripeptide added to the N-terminus of the rabbit  $\alpha$ -Tm<sup>37</sup> and in which Cys190 was mutated to Ile. The cDNA was cloned into vector pET24a<sup>+</sup> for expression in *Escherichia coli*. Mutagenesis was performed by inverse PCR using the KOD-Plus-Mutagenesis Kit (Toyobo Co. Ltd.). Oligonucleotides used for mutagenesis were synthesized and purified by Invitrogen Life Technologies. All of the mutant expression vectors were confirmed by DNA sequencing (ABI PRISM 310 Genetic Analyzer). Protein expression in BL21(DE3) cells and purification of the Tm mutants were performed in accordance with Kluwe *et al.*<sup>38</sup> Protein concentration was determined by absorbance using the following extinction coefficients (0.1%):  $A_{290}=0.63 \text{ cm}^{-1}$  for G-actin,  $A_{280}=0.75 \text{ cm}^{-1}$  for S1,  $A_{280}=0.24 \text{ cm}^{-1}$  for Tm and Tm mutants, and  $A_{280}=0.45 \text{ cm}^{-1}$  for Tn. The following relative molecular masses were used: 42 kDa for actin, 115 kDa for S1, 66 kDa for Tm and Tm mutants, and 69 kDa for Tn.

### Protein labeling

All of the single-cysteine Tm mutants were labeled with IAEDANS, as previously reported.<sup>18</sup> Actins Cys374 and Gln41 were labeled with DABMI and FLC, respectively, as previously reported.<sup>18</sup> F-actin-bound ADP was replaced with TNP-ADP, as previously reported.<sup>18</sup> Details are described in Materials and Methods of Supplementary Information.



### ATPase measurements

The biochemical activity of the labeled Tm was assayed by the  $\text{Ca}^{2+}$ -dependent regulation of acto-S1 ATPase activity. The measurements were performed at 25 °C in 10 mM KCl, 5 mM  $\text{MgCl}_2$ , 2 mM ATP, 20 mM Tris-HCl (pH 7.6), 1 mM DTT, and either 50  $\mu\text{M}$   $\text{CaCl}_2$  for the  $+\text{Ca}^{2+}$  state or 1 mM ethylene glycol bis( $\beta$ -aminoethyl ether) *N,N'*-tetraacetic acid for the  $-\text{Ca}^{2+}$  state. The protein concentrations used were 4  $\mu\text{M}$  F-actin, 0.57  $\mu\text{M}$  Tm, 0.67  $\mu\text{M}$  Tn, and 1  $\mu\text{M}$  S1. The amount of inorganic phosphate released was determined colorimetrically according to the method of Tausky and Shorr.<sup>39</sup>

### Fluorescence measurements

Steady-state fluorescence was measured using a Hitachi F-4500 fluorometer. Time-resolved fluorescence lifetime measurements were performed with an IBH 5000U fluorometer equipped with a 337-nm light-emitting diode light source. The temperature was maintained at 20 °C. Details are described in [Materials and Methods of Supplementary Information](#).

### Fluorescence resonance energy transfer

The efficiency ( $E$ ) of the resonance energy transfer between probes was determined by measuring either the donor fluorescence intensity or the fluorescence lifetime, with the acceptor ( $F_{\text{DA}}$ ,  $\langle\tau\rangle_{\text{DA}}$ ) and without the acceptor ( $F_{\text{D0}}$ ,  $\langle\tau\rangle_{\text{D0}}$ ), as described by Lakowicz:<sup>21</sup>

$$E = 1 - F_{\text{DA}} / F_{\text{D0}} = 1 - \langle\tau\rangle_{\text{DA}} / \langle\tau\rangle_{\text{D0}} \quad (2)$$

where  $\langle\tau\rangle$  ( $=\sum\alpha_i\tau_i$ ) is the lifetime-weighted quantum yield, which is proportional to the area under the decay curve for the lifetime ( $\int_0^\infty I(t)dt$ ). Details are described in [Supplementary Information](#).

In the case of a single donor and either a single acceptor or multiple acceptors, the transfer efficiency is related to the  $i$ th donor-acceptor distance ( $r_i$ ) and Förster's critical distance ( $R_0$ ), where the transfer efficiency is equal to 50%:

$$\sum_i R_0^6 / r_i^6 = (E^{-1} - 1)^{-1} \quad (3)$$

Förster's critical distance ( $R_0$ ; in nm) can be obtained using the following equation:

$$R_0^6 = (8.79 \times 10^{-11}) n^{-4} \kappa^2 Q_0 J \quad (4)$$

where  $n$  is the medium refractive index (1.4),  $\kappa^2$  is the orientation factor,  $Q_0$  is the donor quantum yield without the acceptor, and  $J$  is the spectral overlap integral between the donor emission spectra  $F_D(\lambda)$  and the acceptor absorption spectra  $\epsilon_A(\lambda)$ , which is defined in the following equation:

$$J = \int F_D(\lambda) \epsilon_A(\lambda) \lambda^4 d\lambda / \int F_D(\lambda) d\lambda \quad (5)$$

The quantum yield ( $Q_0$ ) for AEDANS attached to TnI-133 on the reconstituted thin filament with  $\text{Ca}^{2+}$  was 0.27,<sup>20</sup> and the lifetime-weighted quantum yield ( $\langle\tau\rangle$ ) was 13.82 ns. As the lifetime-weighted quantum yields are proportional to the quantum yields, the quantum yields

for AEDANS attached to the five single-cysteine Tm mutants on the reconstituted thin filaments were determined by measuring the lifetime-weighted quantum yields with and without  $\text{Ca}^{2+}$ . The overlap integrals ( $J$ ) were calculated to be  $6.74 \times 10^{14} \text{ M}^{-1} \text{ cm}^{-1} \text{ nm}^4$ ,  $7.54 \times 10^{14} \text{ M}^{-1} \text{ cm}^{-1} \text{ nm}^4$ , and  $18.7 \times 10^{14} \text{ M}^{-1} \text{ cm}^{-1} \text{ nm}^4$  for the AEDANS-Tm/DAB-F-actin, AEDANS-Tm/TNP-ADP-F-actin, and AEDANS-Tm/FLC-F-actin pairs, respectively.  $\kappa^2 = 2/3$  for the calculation of  $R_0$ .

### Simulation of FRET efficiency

For FRET from an excited donor to two acceptors (between a Tn donor and two Tm acceptors), the transfer efficiency calculation has been described in our previous report.<sup>20</sup> Herein, energy is transferred from an excited donor on each Tm chain to acceptors on the five neighboring actin monomers. The transfer efficiency can be calculated according to previous reports.<sup>22,23</sup> With two possibilities for an acceptor on each actin monomer (present or absent), an excited donor has  $2^5 = 32$  possible configurations. Here the labeling ratio of the acceptor ( $A/P$ ) is denoted as  $p$ . The normalized fluorescence intensity ( $F(p)$ ) of the donor on Tm in the presence of acceptors on F-actin (acceptor labeling ratio  $p$ ) was calculated using the following equation:

$$F(p) = \sum_{i=1}^{32} (f_i / f_0) \alpha_i \quad (6)$$

where  $\alpha_i$  is the probability of the  $i$ th configuration obtained by calculating the polynomial distribution.<sup>22,23</sup>  $f_0$  and  $f_i$  are the fluorescence intensities with and without the acceptor, respectively:

$$f_i = f_0 / \left\{ 1 + \sum_{m=1}^n (R_0 / r_m)^6 \right\} \quad (7)$$

where  $n$  is the number of acceptors in the five adjacent actin monomers found in the  $i$ th configuration;  $r_m$  is the distance between the donor and the acceptor, which can be calculated at each orientation of the Tm segment on F-actin in rigid-body translation and rotation; and  $R_0$  is Förster's critical distance.

Because Tm consists of two chains, the fluorescence intensity ( $F_{\text{av}}(p)$ ) of the donors on a single-cysteine Tm mutant is the average of the two donors on both chains. Thus, the transfer efficiency ( $E_{\text{calc}}(p)$ ) at the labeling ratio  $p$  was calculated using the following equation:

$$E_{\text{calc}}(p) = 1 - F_{\text{av}}(p) \quad (8)$$

### Acknowledgements

We thank Dr. Kayo Maeda (Nagoya University) for her gift of the cDNA clone of rabbit skeletal  $\alpha$ -Tm. This study was supported by a Grant-in-Aid for Scientific Research from the Ministry of Education, Science, Sports and Culture of Japan (to M.M.).

## Supplementary Data

Supplementary data associated with this article can be found, in the online version, at [doi:10.1016/j.jmb.2011.10.033](https://doi.org/10.1016/j.jmb.2011.10.033)

## References

1. Ebashi, S., Endo, M. & Ohtsuki, I. (1969). Control of muscle contraction. *Q. Rev. Biophys.* **2**, 351–384.
2. Perry, S. V. (2001). Vertebrate tropomyosin: distribution, properties and function. *J. Muscle Res. Cell Motil.* **22**, 5–49.
3. Kabsch, W., Mannherz, H. G., Suck, D., Pai, E. F. & Holmes, K. C. (1990). Atomic structure of the actin: DNase I complex. *Nature*, **347**, 37–44.
4. Whitby, F. G. & Phillips, G. N. (2000). Crystal structure of tropomyosin at 7 angstroms resolution. *Proteins Struct. Funct. Genet.* **38**, 49–59.
5. Takeda, S., Yamashita, A., Maeda, K. & Maéda, Y. (2003). Structure of the core domain of human cardiac troponin in the  $\text{Ca}^{2+}$ -saturated form. *Nature*, **424**, 35–41.
6. Vinogradova, M. V., Stone, D. B., Malanina, G. G., Karatzaferi, C., Cooke, R., Mendelson, R. A. & Fletterick, R. J. (2005).  $\text{Ca}^{2+}$ -regulated structural changes in troponin. *Proc. Natl Acad. Sci. USA*, **102**, 5038–5043.
7. Holmes, K. C., Popp, D., Gebhard, W. & Kabsch, W. (1990). Atomic model of the actin filament. *Nature*, **347**, 44–49.
8. Lorenz, M., Popp, D. & Holmes, K. C. (1993). Refinement of the F-actin model against X-ray fiber diffraction data by the use of a directed mutation algorithm. *J. Mol. Biol.* **234**, 826–836.
9. Milligan, R. A. & Flicker, P. F. (1987). Structural relationships of actin, myosin and tropomyosin revealed by cryo-electron microscopy. *J. Cell Biol.* **105**, 29–39.
10. Lehman, W., Craig, R. & Vibert, P. (1994).  $\text{Ca}^{2+}$ -induced tropomyosin movement in Limulus thin filaments revealed by three-dimensional reconstruction. *Nature*, **368**, 65–67.
11. Narita, A., Yasunaga, T., Ishikawa, T., Mayanagi, K. & Wakabayashi, T. (2001).  $\text{Ca}^{2+}$ -induced switching of troponin and tropomyosin on actin filaments as revealed by electron cryo-microscopy. *J. Mol. Biol.* **308**, 241–261.
12. Poole, K. J. V., Lorenz, M., Evans, G., Rosenbaum, G., Pirani, A., Craig, R. *et al.* (2006). A comparison of muscle thin filament models obtained from electron microscopy reconstructions and low-angle X-ray fibre diagrams from non-overlap muscle. *J. Struct. Biol.* **155**, 273–284.
13. Squire, J. M. & Morris, E. P. (1998). A new look at thin filament regulation in vertebrate skeletal muscle. *FASEB J.* **12**, 761–771.
14. dos Remedios, C. G. & Moens, P. D. J. (1995). Fluorescence resonance energy transfer spectroscopy is a reliable “ruler” for measuring structural changes in proteins: dispelling the problem of the unknown orientation factor. *J. Struct. Biol.* **115**, 175–185.
15. Miki, M. (2007). Conformational changes in reconstituted skeletal muscle thin filaments observed by fluorescence spectroscopy. *Adv. Exp. Med. Biol.* **592**, 111–123.
16. Tao, T., Lamkin, M. & Lehrer, S. S. (1983). Excitation energy transfer studies of the proximity between tropomyosin and actin in reconstituted skeletal muscle thin filaments. *Biochemistry*, **22**, 3059–3066.
17. Bacchiocchi, C. & Lehrer, S. S. (2001).  $\text{Ca}^{2+}$ -induced movement of tropomyosin in skeletal muscle thin filaments observed by multi-site FRET. *Biophys. J.* **82**, 1524–1536.
18. Miki, M., Hai, H., Saeki, K., Shitaka, Y., Sano, K. I., Maéda, Y. & Wakabayashi, T. (2004). Fluorescence resonance energy transfer between points on actin and the C-terminal region of tropomyosin in skeletal muscle thin filaments. *J. Biochem. (Tokyo)*, **136**, 39–47.
19. Wang, H., Mao, S., Chalovich, J. M. & Marriott, G. (2008). Tropomyosin dynamics in cardiac thin filaments: a multisite Förster resonance energy transfer and anisotropy study. *Biophys. J.* **94**, 4358–4369.
20. Kimura-Sakiyama, C., Ueno, Y., Wakabayashi, K. & Miki, M. (2008). Fluorescence resonance energy transfer between residues on troponin and tropomyosin in the reconstituted thin filament: modeling the troponin–tropomyosin complex. *J. Mol. Biol.* **376**, 80–91.
21. Lakowicz, J. R. (1999). *Principles of Fluorescence Spectroscopy*, 2nd edit. Kluwer Academic/Plenum Publishers, New York, NY.
22. Taylor, D. L., Reidler, J., Spudich, J. A. & Stryer, L. (1981). Detection of actin assembly by fluorescence energy transfer. *J. Cell Biol.* **89**, 362–367.
23. Miki, M., Barden, J. A. & dos Remedios, C. G. (1986). Fluorescence energy transfer between the nucleotide binding site and Cys-10 in G-actin and F-actin. *Biochim. Biophys. Acta*, **872**, 137–141.
24. Miki, M., O'Donoghue, S. I. & dos Remedios, C. G. (1992). Structure of actin observed by fluorescence resonance energy transfer spectroscopy. *J. Muscle Res. Cell Motil.* **13**, 132–145.
25. Flaherty, K. M., McKay, D. B., Kabsch, W. & Homes, K. C. (1991). Similarity of the three-dimensional structures of actin and the ATPase fragment of a 70-kDa heat shock cognate protein. *Proc. Natl Acad. Sci. USA*, **88**, 5041–5045.
26. Xu, C., Craig, R., Tobacman, L., Horowitz, R. & Lehman, W. (1999). Tropomyosin positions in regulated thin filaments revealed by cryoelectron microscopy. *Biophys. J.* **77**, 985–992.
27. Bivin, D. B., Stone, D. B., Schneider, D. K. & Mendelson, R. A. (1991). Cross-helix separation of tropomyosin molecules in acto-tropomyosin as determined by neutron scattering. *Biophys. J.* **59**, 880–888.
28. Saeki, K., Sutoh, K. & Wakabayashi, T. (1996). Tropomyosin-binding site(s) on the *Dictyostelium* actin surface as identified by site-directed mutagenesis. *Biochemistry*, **35**, 14465–14472.
29. Hirono, M., Endoh, H., Okada, N., Numata, O. & Watanabe, Y. (1987). *Tetrahymena* actin: cloning and sequencing of the *Tetrahymena* actin gene and identification of its gene product. *J. Mol. Biol.* **194**, 181–192.
30. Saeki, K. & Wakabayashi, T. (2000). A230Y mutation of actin on subdomain 4 is sufficient for higher

- calcium activation of actin-activated myosin adenosinetriphosphatase in the presence of tropomyosin-troponin. *Biochemistry*, **39**, 1324–1329.
31. Li, X., Tobacman, L. S., Mun, J. Y., Craig, R., Fischer, S. & Lehman, W. (2011). Tropomyosin position on F-actin revealed by EM reconstruction and computational chemistry. *Biophys. J.* **100**, 1005–1013.
32. Tanaka, H. & Oosawa, F. (1971). The effect of temperature on the interaction between F-actin and tropomyosin. *Biochim. Biophys. Acta*, **253**, 274–283.
33. Hiratsuka, T. (1982). Biological activities and spectroscopic properties of chromophoric and fluorescent analogs of adenine nucleoside and nucleotides, 2',3'-O-(2,4,6-trinitrocyclohexadienylidene) adenosine derivatives. *Biochim. Biophys. Acta*, **719**, 509–517.
34. Spudich, J. A. & Watt, S. (1971). The regulation of rabbit skeletal muscle contraction: I. Biochemical studies of the interaction of the tropomyosin-troponin complex with actin and the proteolytic fragments of myosin. *J. Biol. Chem.* **246**, 4866–4871.
35. Weeds, A. G. & Taylor, R. S. (1975). Studies on the chymotryptic digestion of myosin. Effects of divalent cations on proteolytic susceptibility. *Nature*, **257**, 54–56.
36. Ebashi, S., Wakabayashi, T. & Ebashi, F. (1971). Troponin and its components. *J. Biochem. (Tokyo)*, **69**, 441–445.
37. Monteiro, P. B., Lataro, R. C., Ferro, J. A. & Reinach, F. C. (1994). Functional alpha-tropomyosin produced in *Escherichia coli*. A dipeptide extension can substitute the amino-terminal acetyl group. *J. Biol. Chem.* **269**, 10461–10466.
38. Kluwe, L., Maeda, K., Miegel, A., Fujita-Becker, S., Maéda, Y., Talbo, G. *et al.* (1995). Rabbit skeletal muscle  $\alpha$ -tropomyosin expressed in baculovirus-infected insect cells possesses the authentic N-terminus structure and functions. *J. Muscle Res. Cell Motil.* **16**, 103–110.
39. Tausky, H. H. & Shorr, E. (1953). A microcolorimetric method for the determination of inorganic phosphorus. *J. Biol. Chem.* **202**, 675–685.



## Supplemental Information

Miki *et al.* JMB-D-11-00903

### SI Materials and Methods

**Protein Labeling.** All of the single-cysteine Tm mutants were labeled with IAEDANS using the following procedure. The Tm mutants were incubated in 1 mM DTT and 40 mM Tris-HCl (pH 8.0) at 37 °C for 2 h. The pH of the samples was adjusted to 4.5, followed by centrifugation at 20,000 g for 20 min. The pellet was dissolved in 1 M NaCl, 1 mM EDTA, and 40 mM phosphate buffer (pH 7.0). The sample solution was mixed with a 10-fold molar excess of AEDANS at 25 °C for 24 h. The reaction was terminated by the addition of 1 mM DTT. To remove excess AEDANS, the reaction was fractionated with 70% ammonium sulfate and exhaustively dialyzed against 5 mM phosphate buffer (pH 7.0) and 0.1 mM DTT. The sample solution was clarified by centrifugation at 550,000 g for 10 min. The labeling ratios for AEDANS to the Tm mutants were 1.6 ~1.2. Actin Cys374 labeling with DABMI was performed as follows. G-actin (50 µM) was incubated for 6 h at 4 °C with a 10-fold molar excess of DABMI in 0.5 mM ATP, 0.1 mM CaCl<sub>2</sub>, and 2 mM Tris-HCl (pH 8.0). The reaction was stopped by the addition of 1 mM DTT. The sample was centrifuged at 56,000 g for 15 min to remove the unreacted DABMI. The supernatant was polymerized in 0.1 M KCl and 2 mM MgCl<sub>2</sub> and then centrifuged at 100,000 g for 90 min. The pellet was suspended in 1 mM ATP, 0.1 mM CaCl<sub>2</sub>, and 2 mM Tris-HCl (pH 8.0) following dialysis against 0.1 mM ATP, 0.1 mM CaCl<sub>2</sub>, and 2 mM Tris-HCl (pH 8.0). The sample solution was clarified by centrifugation at 550,000 g for 10 min. The labeling ratio of DABMI to actin was usually 1.0. The DAB-F-actin with the labeling ratio of 0.5 was prepared by mixing DAB-G-actin and

nonlabeled G-actin with 1/1 ratio. Actin Gln41 labeling with FLC was performed as follows. G-actin (50 µM) was incubated for 20~40 h at 4 °C with a 2~5-fold molar excess of FLC in 5 mM Tris-HCl (pH 8.0), 0.5 mM ATP, 1 mM DTT, 1 mM NaN<sub>3</sub>, and 1.5 µM transglutaminase. The labeled actin was polymerized in 50 mM NaCl and 2 mM MgCl<sub>2</sub> and then centrifuged at 100,000 g for 90 min. The pellet was suspended in 0.1 M NaCl, 2 mM MgCl<sub>2</sub>, and 0.5 mM DTT and then centrifuged again to remove the unreacted FLC. The labeled actin pellet was suspended in 2 mM Tris-HCl (pH 8.0), 0.1 mM ATP, 0.1 mM CaCl<sub>2</sub>, and 0.25 mM DTT and then dialyzed against the same buffer solution. The labeling ratio of FLC to actin varied from ~0.5 to ~1.0 depending on the amount of FLC added in the reaction and the length of reaction time. Actin labeling with TNP-ADP was performed as follows. The F-actin pellet was dissolved in 60 mM KCl and 10 mM Tris-HCl (pH 8.0), and the solution was re-centrifuged to remove either the free ATP or ADP, as the binding affinity for TNP-ATP is significantly lower than for ATP and ADP. The F-actin pellet was dissolved in 1 mM Tris-HCl (pH 8.0) and 0.1 mM CaCl<sub>2</sub>. The solution was sonicated on ice for up to 20 s using a Tomy UD-201 sonicator and followed by an immediate addition of 1 mM TNP-ATP; then the solution was sonicated again. The sample solution was incubated in 60 mM KCl, 2 mM MgCl<sub>2</sub>, and 10 mM Tris-HCl (pH 8.0) and then centrifuged again. The F-actin pellet was dissolved in 1 mM Tris-HCl (pH 8.0) and 0.1 mM CaCl<sub>2</sub>. The sample solution was sonicated, supplemented with 1 mM TNP-ATP, and sonicated again. The TNP-ATP-G-actin polymerized into TNP-ADP-F-actin in 60 mM KCl, 2 mM MgCl<sub>2</sub>,

1 mM DTT, 2 mM NaN<sub>3</sub>, and 10 mM Tris-HCl (pH 8.0). The sample was centrifuged, and the pellet was re-dissolved in the same buffer solution and re-centrifuged until all of the unbound TNP-ATP/ADP was removed. The TNP-ADP-F-actin was stabilized by adding a 1.2-fold molar excess of phalloidin. The labeling ratio of TNP-ADP to actin varied from ~0.3 to ~0.6 in different preparations. To determine the labeling ratios, the following absorption coefficients were used: 24,800 M<sup>-1</sup> at 460 nm for DABMI, 6100 M<sup>-1</sup> at 337 nm for AEDANS, and 26,400 M<sup>-1</sup> at 408 nm for TNP-ADP. The protein concentration of the labeled actin was determined using the Pierce BCA protein assay reagent.

***Time-resolved fluorescence lifetime measurements.*** In the multiexponential model, the intensity is assumed to decay as the sum of individual single-exponential decays:

$$I(t) = \sum_{i=1}^n \alpha_i \exp(-t/\tau_i) \quad (\text{eq. 1})$$

The lifetime-weighted quantum yield was given by

$$\langle \tau \rangle = \sum_{i=1}^n \alpha_i \tau_i \quad (\text{eq. 2})$$

For a double-exponential decay it becomes

$$\int_0^{\infty} I(t) dt = \alpha_1 \tau_1 + \alpha_2 \tau_2 \quad (\text{eq. 3})$$

$\langle \tau \rangle$  is proportional to the area under the decay curve of the lifetime, so that it is called as a lifetime-weighted quantum yield. The transfer efficiencies were determined by the lifetime-weighted quantum yield ( $\langle \tau \rangle = \sum \alpha_i \tau_i$ ) with ( $\langle \tau \rangle_{DA}$ ) and without ( $\langle \tau \rangle_{D0}$ ) the acceptor.

$$E = 1 - \langle \tau \rangle_{DA} / \langle \tau \rangle_{D0} \quad (\text{eq. 4})$$

Figure S2 shows the time-resolved fluorescence intensity decay curves of AEDANS attached to residue 167 of the single-cysteine mutant Tm in the presence and absence of the acceptor-DABM attached to Cys374 of actin. The decays were measured with an excitation at 337 nm and emission at 490 nm. A sharp cut-off filter, SC-42 (Fuji Film) was placed on the emission side. Decay curves were analyzed by DAS6 fluorescence decay analysis software.

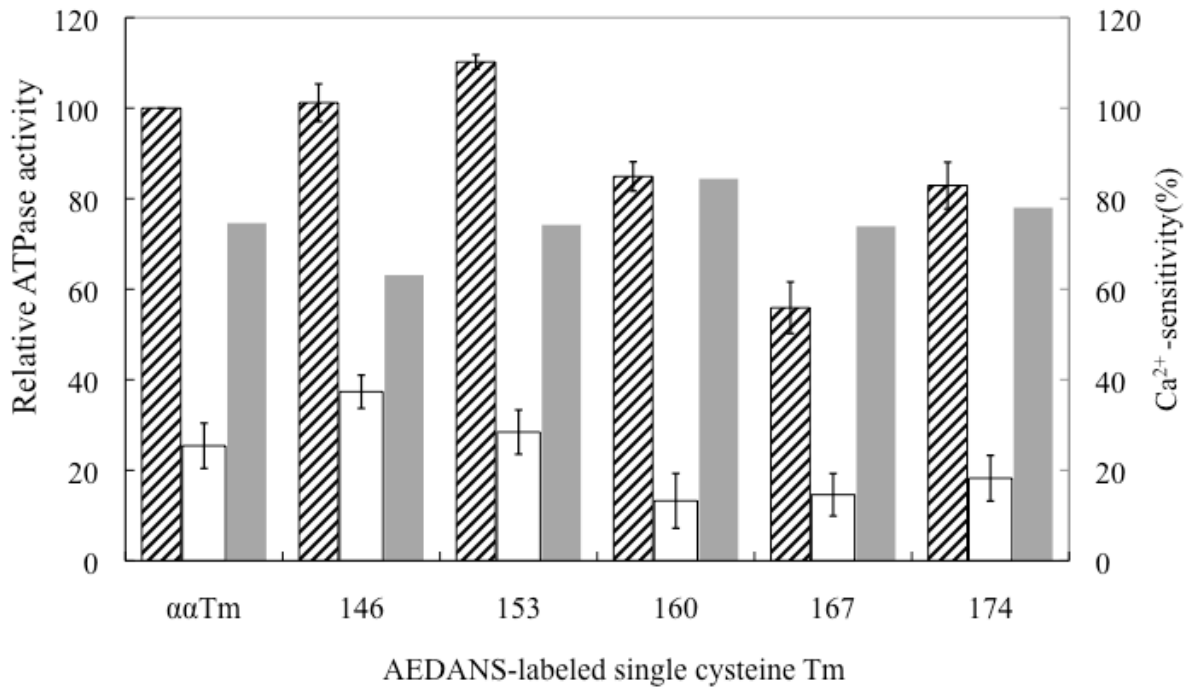


**Figure S1.** Ca<sup>2+</sup>-dependent regulation of actoS1-ATPase by the labeled Tm mutants. The reactions were carried out at 25 °C with 4 μM F-actin, 1 μM rabbit skeletal S1, 0.57 μM Tm and 0.67 μM Tn in 10 mM KCl, 5 mM MgCl<sub>2</sub>, 1 mM DTT, 2 mM ATP and 20 mM MOPS (pH 7.0) in the presence of 50 μM CaCl<sub>2</sub> (hatched bar graphs) or 1 mM EGTA (open bar graphs). The ATPase activity of actoS1 and Tn with each labeled Tm mutant was always compared with that of actoS1 and Tn with native Tm under the same experimental conditions. All ATPase activities were measured more than three times. The ordinate value of 100 (%) represents the ATPase activity of actoS1 and Tn with native Tm in the presence of Ca<sup>2+</sup>. The Ca<sup>2+</sup> sensitivities defined as  $\{1 - (\text{Activity}_{-\text{Ca}} / \text{Activity}_{+\text{Ca}})\} \times 100$  were also shown (grey bar graphs).

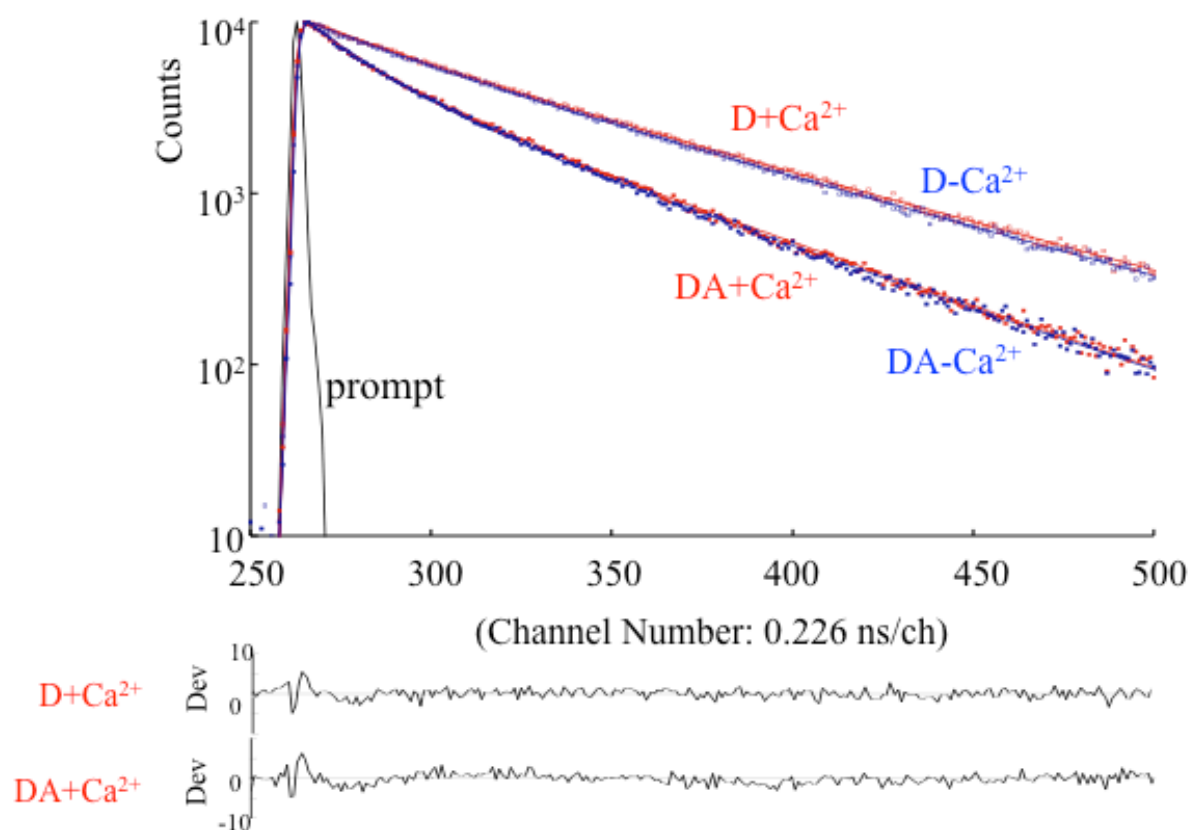


**Figure S2.** Fluorescence intensity decay curves for the donor-AEDANS attached to Tm Cys167 in the reconstituted thin filaments with (red) and without (blue)  $Ca^{2+}$ . The sharp peak on the left is from the excitation light pulse. The blank and filled square plots are the fluorescence intensity decay curves for the donor with and without the acceptor-DABM attached to actin Cys374, respectively. The smooth lines are the decay curves calculated with two exponential lifetimes. The residual plots of the fit are displayed in the lower space across the figure. The samples (5.9  $\mu$ M actin, 0.76  $\mu$ M Tm, and 0.87  $\mu$ M Tn) were measured in buffer F with either 50  $\mu$ M  $CaCl_2$  (+Ca) or 1 mM EGTA (–Ca).

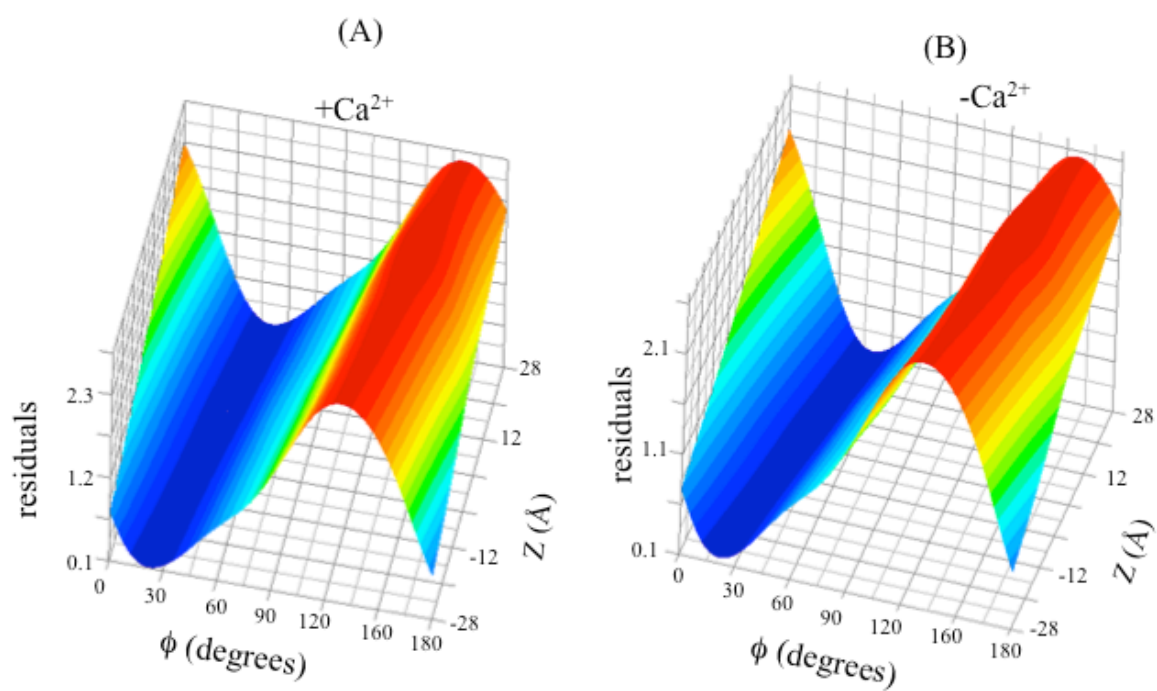


**Figure S3.** A three-dimensional map of the residuals as a function of  $\phi$  and  $Z$  in the presence (A) and absence (B) of  $Ca^{2+}$ , with the constant values of  $R=41$  Å and  $\theta=-21^\circ$  (A), or  $R=40$  Å and  $\theta=-17^\circ$  (B).

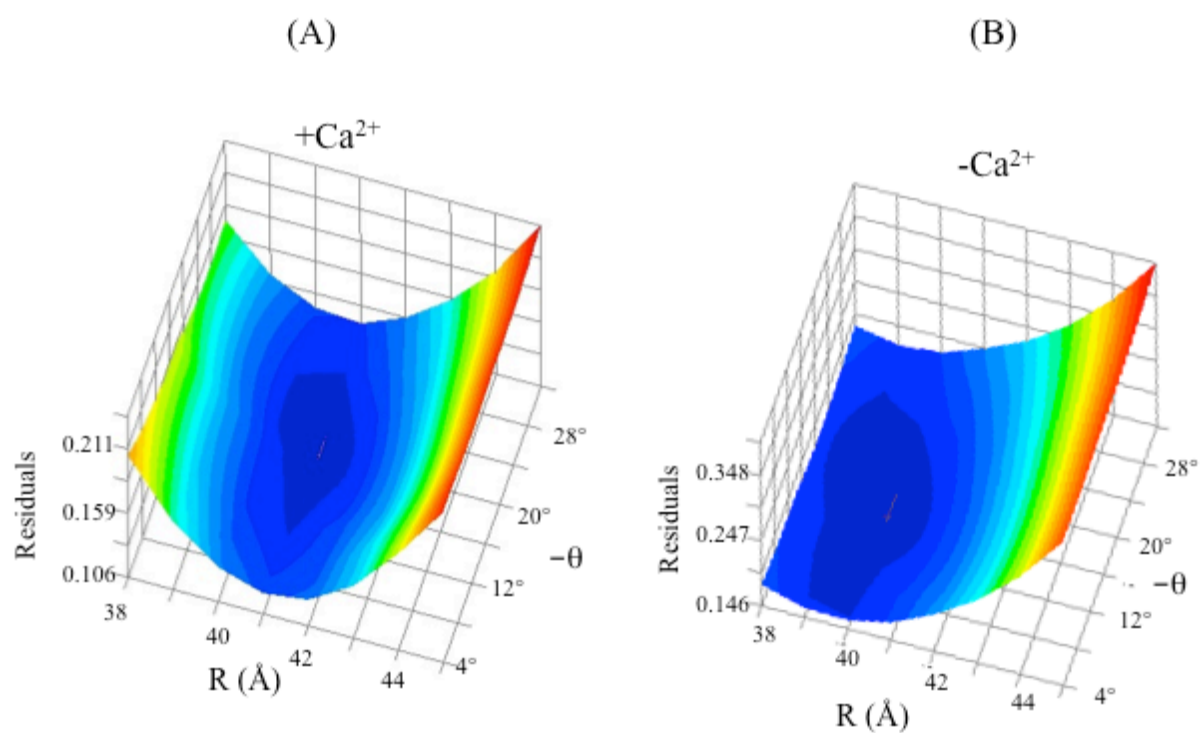


**Figure S4.** A three-dimensional map of the residuals as a function of  $R$  and  $\theta$  in the presence (A) and absence (B) of  $Ca^{2+}$ .



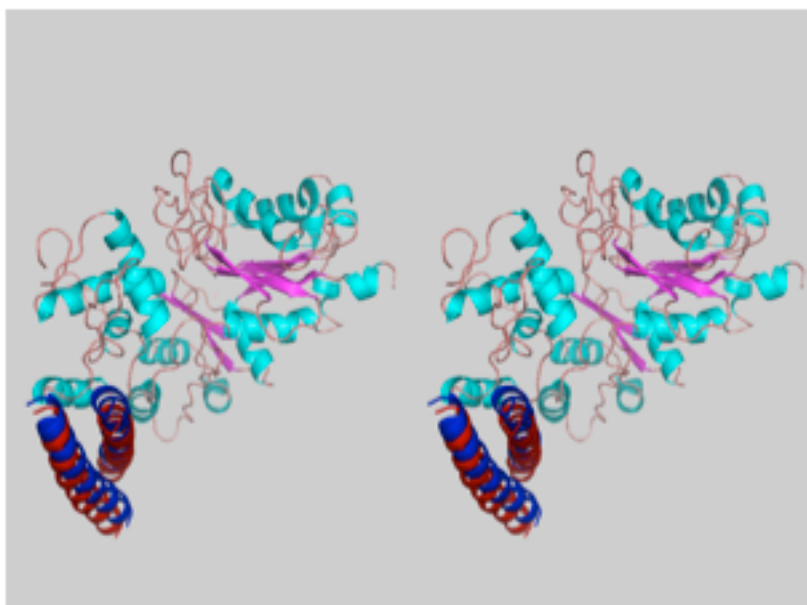


**Figure S5.** A stereo view of Tm segment 251–279 on actin in the presence (red) and absence (blue) of  $\text{Ca}^{2+}$ . Actin helices 223–230 and 309–320 are close to the Tm segment.